Nafar Dastgerdi, Jairan; Jaberi, Omid; Remes, Heikki

Influence of internal and surface defects on the fatigue performance of additively manufactured stainless steel 316L

Published in:
International Journal of Fatigue

DOI:
10.1016/j.ijfatigue.2022.107025

Published: 01/10/2022

Document Version
Publisher's PDF, also known as Version of record

International Journal of Fatigue 163 (2022) 107025

Contents lists available at ScienceDirect

International Journal of Fatigue

journal homepage: www.elsevier.com/locate/ijfatigue

Influence of internal and surface defects on the fatigue performance of additively manufactured stainless steel 316L

Jairan Nafar Dastgerdi [a,b,*], Omid Jaberi [a], Heikki Remes [b]

[a] Department of Aerospace Engineering, Amirkabir University of Technology (Tehran Polytechnic), 424 Hafez Avenue, Tehran, Iran
[b] Department of Mechanical Engineering, School of Engineering, Aalto University, P.O. Box 14300, FIN-00076 Aalto, Finland

ARTICLE INFO

Keywords:
Additive manufacturing
Defects
Surface roughness
X-ray computed tomography
Fatigue life

ABSTRACT

The additive manufacturing (AM) process generates new material challenges with associated features like internal defects and inherent surface roughness, reducing fatigue performance. This paper introduces a new approach to characterizing internal defects and surface irregularities of additively manufactured stainless steel 316L samples using X-ray computed tomography (XCT). This method overcomes the limitations of previous methods and can effectively provide holistic information on the surface topologies of AM components. An equivalent defect size, $\sqrt{area_{eff}}$, based on defects' features and the interaction of internal and surface imperfections, is proposed for fatigue life and failure origins prediction.

1. Introduction

Metal AM is overgrowing as a disruptive technology with the capability of revolutionizing how products from different industrial sectors such as aerospace, automotive, marine, and biomedical are designed. It has developed as an innovative and reliable manufacturing process that directly produces the CAD model's component [1–3]. Despite the advantages of AM techniques and increasing demands in different industries, they are still not fully adopted in various engineering practices. Diversity in the mechanical performance of metal AM parts due to variation in microstructure and defect characteristics is a continuing challenge [4,5]. Metal AM components usually undergo complex cyclic thermal history consisting of directional heat extraction, repeated melting, and rapid solidification [6,7], which would create anisotropic microstructures (columnar grains along building direction) and residual stress in the manufactured parts [8]. AM internal defects such as lack of fusion layers, and gas pores are also generated either due to insufficient energy, or excessive energy during metal AM process [9]. The inherent repetitive nature of the build process along with the half-fused particles attached to the surface and the presence of surface-connected defects result in a highly rough surface for metal AM components [10].

Internal defects and surface defects or roughness have been recognized as the most critical fatigue damage initiation sites specifically in Powder Bed Fusion (PBF) parts. Variations in surface roughness and defect characteristics such as size, shape, location, and interactions have been identified as the primary sources of scatter and uncertainty in the fatigue performance of AM metals [11–18]. Although, for a thorough description of the fatigue strength, other secondary factors (microstructure and residual stresses) should also be considered. With the hypothesis of a nearly homogeneous microstructure and low residual stresses, the impact of these variables becomes small to that of the internal and surface defects. Residual stresses can be relieved by post-heat-treatment or sensibly decreased by imposing a controlled cooling by pre-heating the platform [19,20]. The role of microstructure is essential for crack propagation in the presence of very small defects and energy dissipation during fatigue crack propagation. However, the fatigue limit is not sensibly influenced by the microstructure when the defect size is larger than the grain size, especially in the case of ductile materials [5]. Defects exist even in the case of optimized manufacturing parameters with prevalent AM technology, and they can effectively result in failures of AM parts, particularly in fatigue-critical engineering practices. Therefore, standardized test procedures to gain non-destructive insights into the quality of AM parts are being developed [21,22]. While surface topology has been reliably controlled in traditional manufacturing techniques, as-built surfaces in AM fabricated parts are comparatively complex, and post-build machining has diminished the business case for AM. This has raised an issue for applications in different industries where fatigue performance is an essential consideration. Surface or near-surface defects cannot be eliminated, and improving the fatigue performance of net-shaped AM parts with minor post-processing is an operational challenge. Hence, powerful techniques and analysis

* Corresponding author.
E-mail address: jairan.nafardastgerdi@aalto.fi (J. Nafar Dastgerdi).

https://doi.org/10.1016/j.ijfatigue.2022.107025
Received 17 February 2022; Received in revised form 19 May 2022; Accepted 20 May 2022
Available online 25 May 2022

Nomenclature

Abbreviations

AM	Additive manufacturing
PBF	Powder bed fusion
XCT	X-ray computed tomography
SEM	Scanning electron microscopy

Symbols

$\sqrt{area_{eff}}$	Equivalent defect size
$\sqrt{area_{D}}$	Prospective internal defect size
$\sqrt{area_{R}}$	Equivalent surface roughness defect size
d_{R-D}	The shortest distance between two adjacent defects
R_v	The deepest valley of the surface profile
R_a	The roughness average
R_z	The average maximum height of surface profile
$\sqrt{area_{eff,max}}$	The maximum critical effective defect size
σ_{wl}	The lower bound of the fatigue limit
HV	Vickers hardness
Δk_{th}	Threshold stress intensity factor range
$area_{st}$	The size of the stable crack growth zone
$f(x)$	Frechet distribution function
α, β	Shape and scale parameters

approaches are required to detect and characterize AM defects, especially for the risky-engineering components fabricated by AM. It might be challenging to achieve the quantitative characterization of spatial distribution and real morphology of AM defects only using traditional methods [23–25]. The traditional tools such as tactile and optical profilometers and laser scanners work only on the exterior surfaces of parts and often only in lines or on flat surfaces. Thus, it is impossible to generally measure the surface topography of internal surfaces of complex AM parts such as struts in lattices [26].

XCT is a unique and powerful non-destructive method to evaluate heterogeneous material microstructure in 3D [27,28]. XCT is recently used in AM to obtain a distinct analysis of internal material imperfections, especially the porosity and defect of AM specimens [29–31]. For this purpose, suitable image analysis methods and sequences are needed to characterize porosity and internal defects from XCT reconstructions [32,33]. In addition, XCT reconstructions provide valuable data and information for the statistical competency of metal AM components [34]. As the characteristics of surface defects and surface topography significantly influence components' trustworthiness and fatigue performance [35–37], the XCT technique has also been recently employed to thoroughly identify the features of the surface defects of the metal AM components [38–42]. However, there is still a gap in the determination algorithm to systematically characterize the surface defects of complex metal AM parts with low computational cost and minimum possible error in image processing. This study is an attempt to fill this gap.

Plessis and Beretta [42] have presented a notch-based surface roughness evaluation method using XCT data. They have proposed to fit a cylinder geometry element to the exterior surface of the before scan data and create a duplicate of this cylinder. The original surface was compared to the best-fit cylinder volume, and the result was analyzed using a nominal-actual comparison illustrating maximum deviations between the rough surface and the fitted cylinder to define the notches. However, their approach presented local information about the surface defects, mainly focusing on the killer notches; this method still has two limitations. First, the connectivity between surface notches depends on the depth of the notches, and therefore a depth criterion for defining the notches as defects depends on the surface condition and is a manual step that the user detects. Second, this approach is primarily employed to visualize and interpret notch geometry relative to crack location. However, they have reported that some notches may not be detected using this approach. It should be noted that the surface profiles for each section have some peaks and valleys, and the deviation from the center (mean) axis should be considered a criterion for notch detection. The new proposed approach mathematically calculates the center axis and then determines the notches and depth of the valleys. All steps have been carried out systematically using the determination algorithm applied to the XCT data. This proposed method can also provide global and local information on the surface roughness using quantitative parameters (e.g., Ra and Rz).

Indeed, this study introduces a new approach to characterizing complex defects and surface topologies using XCT data. This approach has precisely studied characteristics of internal defects such as size/volume, shape, location (distance from the surface), and spatial distribution along the sample and around its axis to evaluate and quantify their effects on the fatigue performance of these materials. Moreover, it has analyzed data from the 3D scan to characterize the surface defects (irregularities) and then detect the critical surface roughness profiles and potential sites for fatigue crack initiation on the surface. The proposed method also investigates the effect of internal and surface defects on the fatigue performance of metal AM samples. Therefore, it can describe all of the typical fatigue-critical features introduced by AM processes. The stainless steel 316L is frequently used in energy, automotive, and medical industries because of its excellent corrosion properties, formability, and high strain-hardening rates. Metal AM technologies have been substantially developed in the past years to evaluate manufacturability and mechanical properties of additively manufactured parts [43]. This work studied the fatigue performance of stainless steel 316L specimens additively manufactured with different processing strategies (layer thicknesses and built directions).The roughness of the inclined surface is related to layer thickness [44]. Moreover, the total porosity is usually correlated to the average process energy applied per volume of material and is described by energy density, a ratio between laser power, scanning velocity, hatch distance, and layer thickness [45]. Indeed, layer thickness influences both internal and surface defects, and thus, it has been chosen in this study as a variable of process parameters.

This paper focuses mainly on the capability to predict the fatigue resistance of AM parts as a frequently relevant open issue. Defect-based fatigue life prediction models have been of great interest, especially for metal AM par. However, most previous studies have only considered the internal defect size due to some limitations in surface defect characterization [8,46–48]. Recently, Sanaei and Fatemi proposed an equivalent parameter (a combination of the maximum prospective internal defect size and the maximum prospective equivalent surface defect size) using Murakami's approach [49] for estimation of the initial defect size [50]. However, the interaction effect of internal and surface defects has not been considered. Moreover, the effective defect size based on the roughness profile has been measured using stylus surface profilometry results with the limitation in catching some critical features of surface profiles [51]. Due to the nature of surfaces produced by AM, the maximum prospective equivalent surface defect size parameter may not accurately represent the crack-like notches out of reach in the stylus method or 3D optical profilometry [52]. Thus, it is necessary to establish a more accurate standard definition of the effective defect size based on the extended 3D analysis considering the surface effect. In this paper, the critical equivalent defect size parameter, $\sqrt{area_{eff}}$, has been introduced to consider the influence of internal and surface defects and their interactions on the fatigue performance of metal AM parts using the new 3D defects (internal and surface) determination algorithm. This paper reveals that the proposed defects characterization approach can predict specific locations on the surface prone to initiating fatigue failure. Based on 3D defects and surface topography analysis of intact specimens (before fatigue testing), the predicted multi-fatigue origins are in good agreement with those obtained from the experiments and the

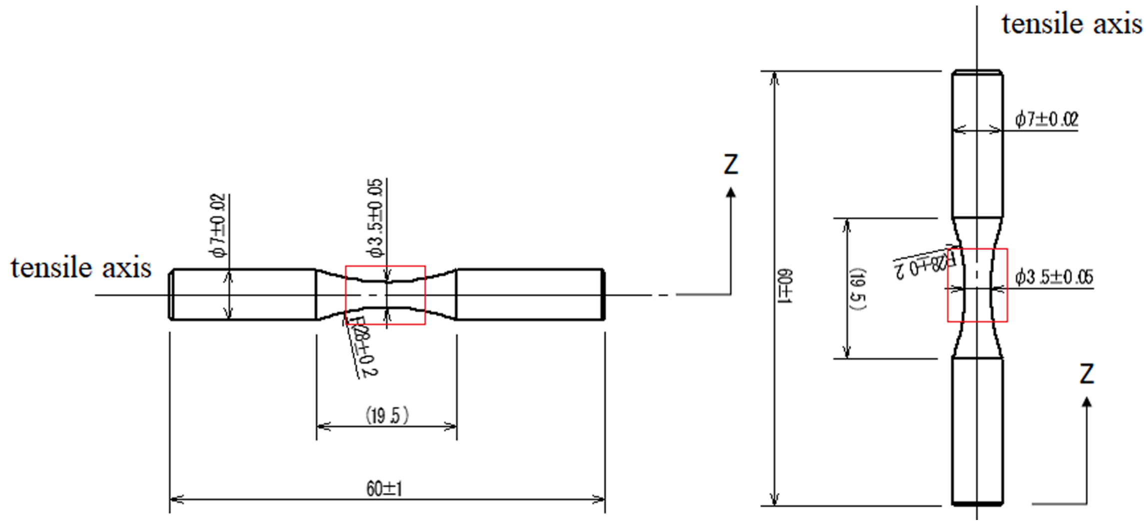

Fig. 1. Configuration of the manufactured fatigue specimen.

fractography. Indeed, anticipating from which defect of the thousands detected the failure will originate, would allow estimating the fatigue limit of the material without laborious experimental testing. This study also assists in the characterization and control of process-related defects and irregularities and their influence on component durability. This is one of the main areas of concern, and it should be rigorously addressed for the qualification and certification of metal AM components.

2. Material and methods

2.1. Material and specimen fabrication

In this paper, the studied material is stainless steel 316L produced by metal 3D printing of EOS GmbH (M290) using direct metal laser sintering as a PBF method. Two types of hour-glass-shaped round specimens have been manufactured: (1) samples fabricated with its tensile axis parallel to the z-direction (vertical sample), (2) the other samples fabricated with its tensile axis perpendicular to the z-direction (horizontal sample). All specimens were made at the 250 W power capability of the machine. The scanning speed was approximately 1083 mm/s. The hatch distance was 0.09 mm. According to equation $E_a = \frac{P}{vht}$ (E_a.P.v.h. and t are energy density per unit volume, beam power (W), beam velocity (mm/s), hatch spacing or line offset (mm) which is the spacing between melt tracks, and layer thickness (mm)) the volumetric energy density was calculated 64.12 J/mm^3. The powder is spherical and about 37 µm in diameter. Two types of specimens with different layer thicknesses, 20 µm and 40 µm, were fabricated. The platform was pre-heated and retained at a constant 80^{oC} during the print. None of the parts received any final heat treatment; however, significant residual stresses were not expected owing to the platform pre-heating [53]. This study has been carried out with the hypothesis of low residual stresses. All fatigue specimens were built to net shape, meaning no post-process machining would be performed. The dimensions of horizontal and vertical samples are shown in Fig. 1.

2.2. Fatigue testing

Load-controlled uniaxial fatigue testing was performed on the horizontal and vertical samples. A frequency of 10 Hz and an R-ratio of 0.1 was employed during testing. Samples were tested to be fractured. Fracture surface analysis of the failed fatigue samples was performed from the top and front view of samples using scanning electron microscopy (SEM).

2.3. X-ray microtomography and 3D defect characterization

2.3.1. X-ray microtomography

The XCT images of the intact specimen before the fatigue test were captured using General Electric (GE) phoenix v|tome|x s machine with 5 µm pixel size. The X-ray tube acceleration voltage and power were set to 170 kV and 5.1 W, respectively. A 0.5 mm copper filter was used to absorb low-energy X-rays unnecessary for imaging. 2000 projection images over 3600 of rotation were acquired with 5 s exposure time per angular position. The detector first waited for a single exposure time at every angle and then took an average of over two or three exposures. XCT imaging was carried out from the middle of the specimens with a length of 10 mm, as depicted with a red rectangular in Fig. 1. The micro-CT scans for horizontally and vertically manufactured samples with different layer thicknesses were performed to study the variability analysis of defects and surface topographies.

2.3.2. 3D defect and surface roughness characterization

Results of micro-CT of specimens and generated data on internal defects volume and position using ThermoFisher PerGeos software have been used for analysis in this study. The internal defect determination algorithm has been extended to characterize internal defects' projected area, sphericity, and distance from the surface. In addition, variabilities of the characteristics of the internal defects have been studied throughout the specimens with respect to the height of the sample and around the sample axis. Defects on the surface usually referred to as surface roughness, are the other type of defects that should be characterized. A rough surface is intrinsic to AM due to the layer-by-layer nature often the build process and is influenced by various parameters. Thus, surface roughness characterization is imperative in metal AM components' fatigue performance. Note that sometimes the defect recognition software cannot recognize the surface defects when they are in touch with the external environment, and there is no difference in the gray level. The new surface defects determination algorithm has been introduced to solve this problem in this study. In this approach, binarization has transformed a gray-level image into a binary image. Then, internal defects (pores) have been excluded, and the edge of the sample is specified. Using the proposed algorithm, the edge data along the height of the sample at different angles can provide the surface roughness profile.

2.4. Quantitative analysis of the effect of defect size on fatigue life

A typical representative dimension for a defect is the parameter

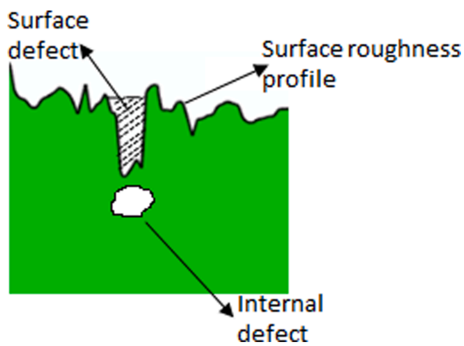

Fig. 2. The combination of internal and surface defects in form of an effective initial crack size.

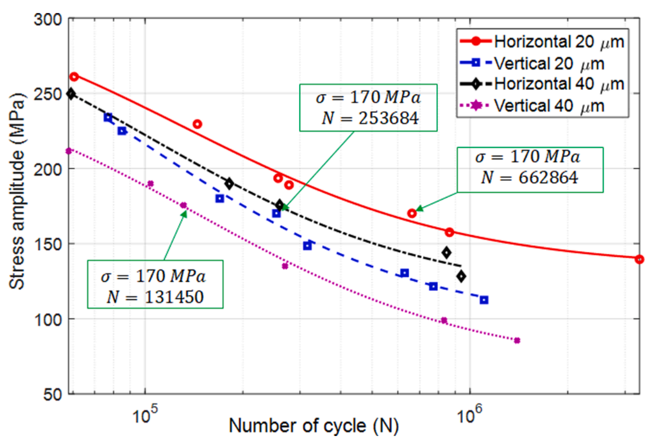

Fig. 3. Fatigue Stress-Life curve for steel 316L specimens fabricated in different building directions with various layer thicknesses.

introduced by Murakami and Endo [52], which has been applied in many works to calculate the stress intensity factor, its threshold value, and the fatigue strength of parts containing defects including AM parts [46–49]. This geometrical parameter reportedly allows calculating the maximum stress intensity factor along the front of an internal or surface crack with the irregular shape when the crack grows perpendicular to the maximum principal stress direction [47]. The lower bound of the fatigue limit σ_{wl} based on $\sqrt{area}$ can be determined by the following equation [54]:

$$\sigma_{wl} = \frac{1.43(HV+120)}{\left(\sqrt{area}\right)^{1/6}}\left[\frac{1-R}{2}\right]^{\alpha} \tag{1}$$

where HV (kgf/mm^2) is Vickers hardness, $R = \sigma_{min}/\sigma_{max}$ and $\alpha = 0.226 + HV \times 10^{-4}$.

In the presence of both internal and surface defects, the interaction effect between them should be considered, e.g. Fig. 2. $\sqrt{area_{eff}}$ can present the incorporation of internal defects and surface roughness as an effective initial crack size. If the space between two adjacent defects is smaller than the size of the smaller defect, the effective defect size must be evaluated by summing the sizes of two defects together and additionally the space between these two defects [54]. Thus, $\sqrt{area_{eff}}$ can be defined as bellow:

$$\sqrt{area_{eff}} = \sqrt{area_D} + \sqrt{area_R} + d_{R-D} \tag{2}$$

where $\sqrt{area_D}$, $\sqrt{area_R}$ are the prospective internal and equivalent surface roughness defect size, respectively. d_{R-D} is the shortest distance between two adjacent defects.

Recently, it has been reported that the calculated equivalent surface roughness defect size $\sqrt{area_R}$ is very close to the value of the R_v parameter which represents the deepest valley of the surface profile [49]. It has been also suggested that R_v is an appropriate parameter to be used as the initial defect size for fatigue life prediction of as-built surface AM metals [15,54]. Thus, the critical equivalent defect size, $\sqrt{area_{eff}}$, can be re-written as.

$$\sqrt{area_{eff}} = \sqrt{area_D} + R_v + d_{R-D} \tag{3}$$

3. Results and discussion

This paper focuses on the uniaxial fatigue performance of the specimens with as-built surfaces and its relationship with detrimental features, e.g., internal defects (pores) and surface defects (surface roughness). Fatigue performances of samples with different processing parameters leading to various surface roughness conditions and internal pores characteristics have been compared. Fig. 3 depicts the stress-life diagram of steel 316L specimens fabricated in different building directions (vertical and horizontal samples) with various layer thicknesses (20 μm and 40 μm). It can be seen the horizontal specimens have better fatigue performance compared to vertical ones and the smaller layer thickness show higher fatigue strengths relative to the bigger layer thickness. The differences are noticeable in both short life and long life regimes. The detrimental effects of defects and surface topographies have been evaluated using the proposed characterization approaches to shed more light on the correlation between the differences in the fatigue performance of these materials and detrimental features. First, the

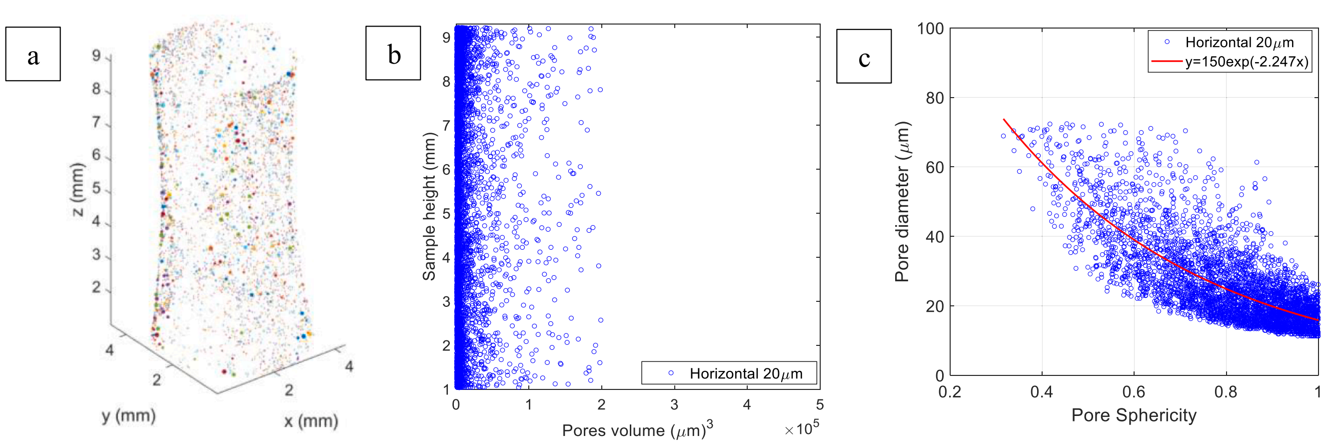

Fig. 4. (a) 3D rendering of internal defects, (b) pores' volume size distribution along the height of the sample and (c) diameter of the pores as a function of sphericity of horizontally fabricated sample with layer thickness 20 μm.

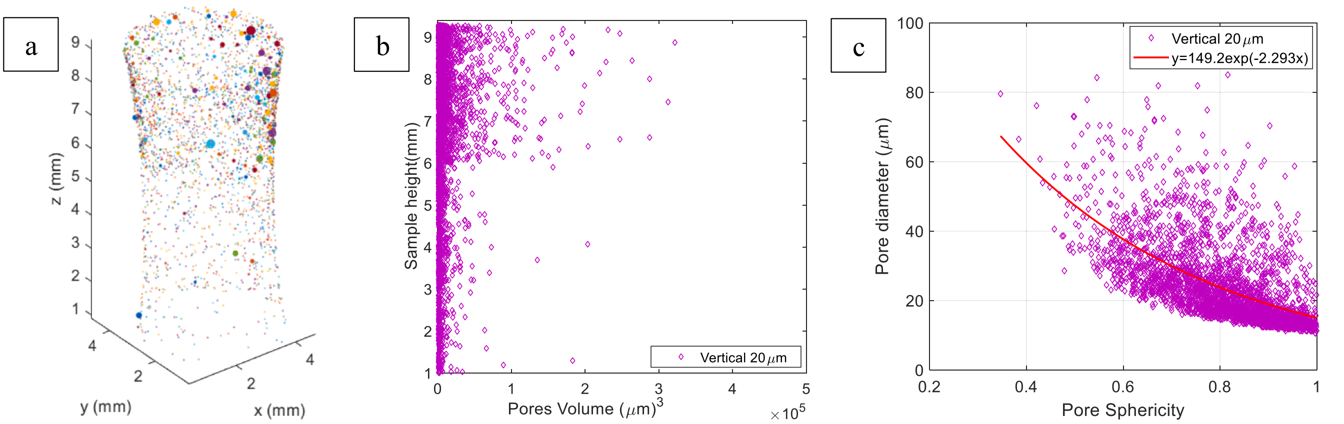

Fig. 5. (a) 3D rendering of internal defects, (b) pores' volume size distribution along the height of the sample and (c) diameter of the pores as a function of sphericity of vertically fabricated sample with layer thickness 20 μm.

variability of internal defects (pores) related to the processing parameters has been studied. Then, the surface roughness characterization using the new proposed approach was carried out. In this study, three samples with different building directions and layers of thicknesses were scanned before fatigue testing. First, defects and surface topographies characterization has been performed. Then, they have tested at the same stress level. The fatigue results for these three samples have been depicted within green rectangular in Fig. 3. It can be seen there is a significant difference between horizontal and vertical samples with a layer of 20 μm. This is an indication of the anisotropic fatigue resistance of metal AM parts. There is also a considerable difference between vertical samples with different layers of thicknesses. The comparison of fatigue lives shows the impact of the build orientation and layer thickness on the fatigue performance of metal AM parts. The following sections investigated the correlation between defects (internal and surface) characteristics and the fatigue performance of as-built AM parts.

3.1. Analysis of variability in internal defect characteristics

In this study, the internal defect characteristics (volume, diameter, sphericity, and projected area) distributions have been compared for specimens with various layer thicknesses (20 μm and 40 μm) and different building directions (horizontal and vertical). Fig. 4a-c depicts the 3D rendering of internal defects (pores), volume size distribution along the height of the sample, and diameter of pores as a function of sphericity for the horizontal sample with a layer of 20 μm, respectively. Fig. 5a-c and 6a-c show the same information for vertical samples with a layer of 20 μm and 40 μm, respectively. A clear difference can be observed between the vertical and horizontal samples. The variability along the build direction shows a specific trend in the scanned height for the size and location of the defects. The defects' population has not been distributed uniformly along the height of the sample, and it depends on the build direction. For vertically fabricated samples, pores have concentrated on the upper side along the build direction; however, they have distributed uniformly for the horizontally manufactured sample. The pores' volume size distribution shown in these figures has illustrated a relationship between pores' volume size, build direction, and layer thickness. The vertically fabricated samples have higher pores' volume size than the horizontally fabricated sample. Moreover, the vertical sample with a layer thickness of 40 μm has internal pores with a higher volume size.

Apart from pores' volume size and diameter, the shape of internal pores is also important to the metal structural behaviour. Defect morphology is usually represented by sphericity. These figures show that the smaller pores have higher sphericity (closer to 1), while the large pores have low sphericity (i.e., high aspect ratio). Low sphericity indicates irregularity in pore shape. Therefore, pores with lower sphericity probably serve as deleterious defects, reducing mechanical performance of metal AM components. The characteristics of internal defects such as their type, location, shape, size, orientation, and density are greatly influenced by the process parameters. The pore size, shape (near-spherical to irregular), and densification can be varied by changing the melting pool size and overlapping between neighboring melt pools [55]. For vertical up deposition direction, due to gravitational

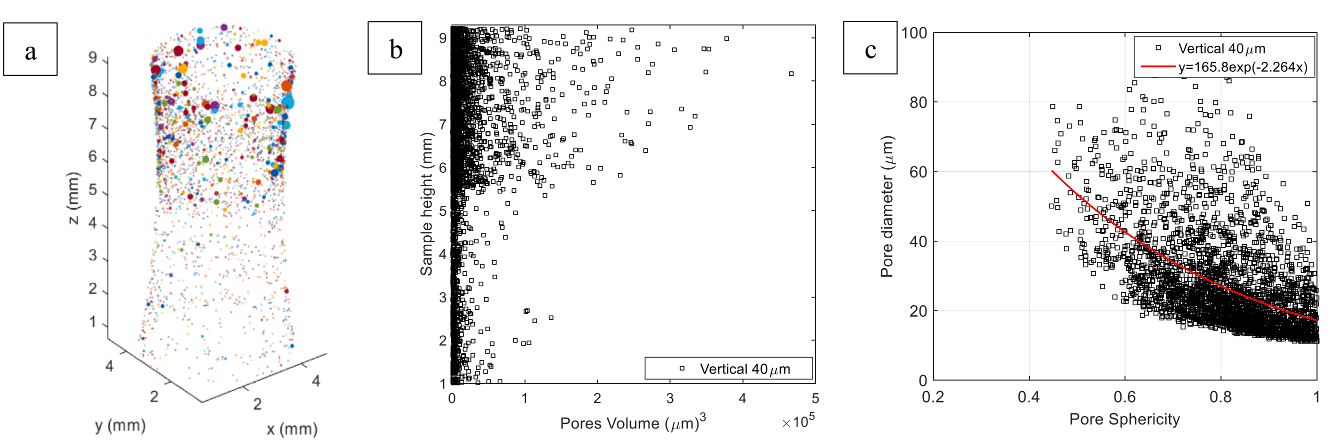

Fig. 6. (a) 3D rendering of internal defects, (b) pores' volume size distribution along the height of the sample and (c) diameter of the pores as a function of sphericity of vertically fabricated sample with layer thickness 40 μm.

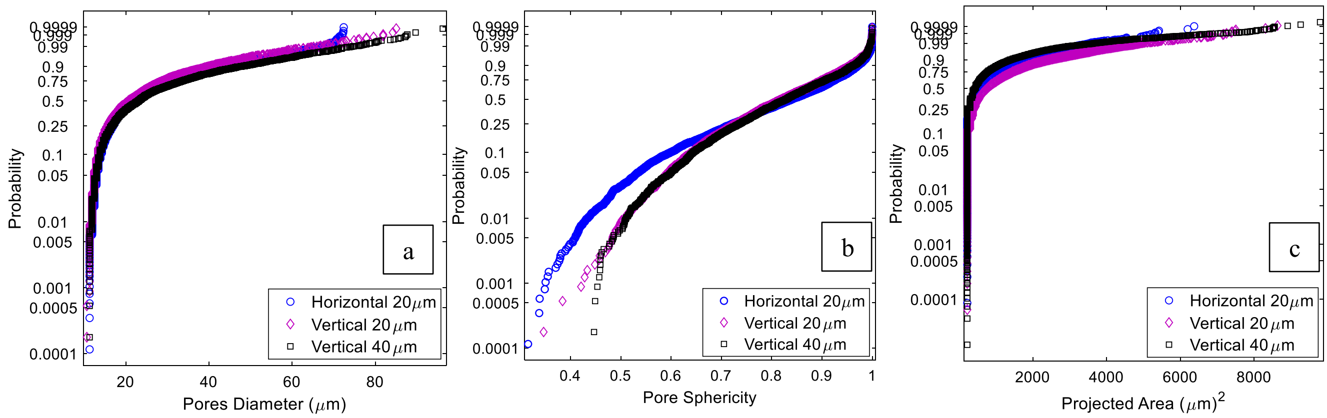

Fig. 7. Comparisons of the (a) equivalent pores' diameter, (b) sphericity, and (c) projected area distributions for horizontal and vertical samples with different layer thickness using extreme value probability plots.

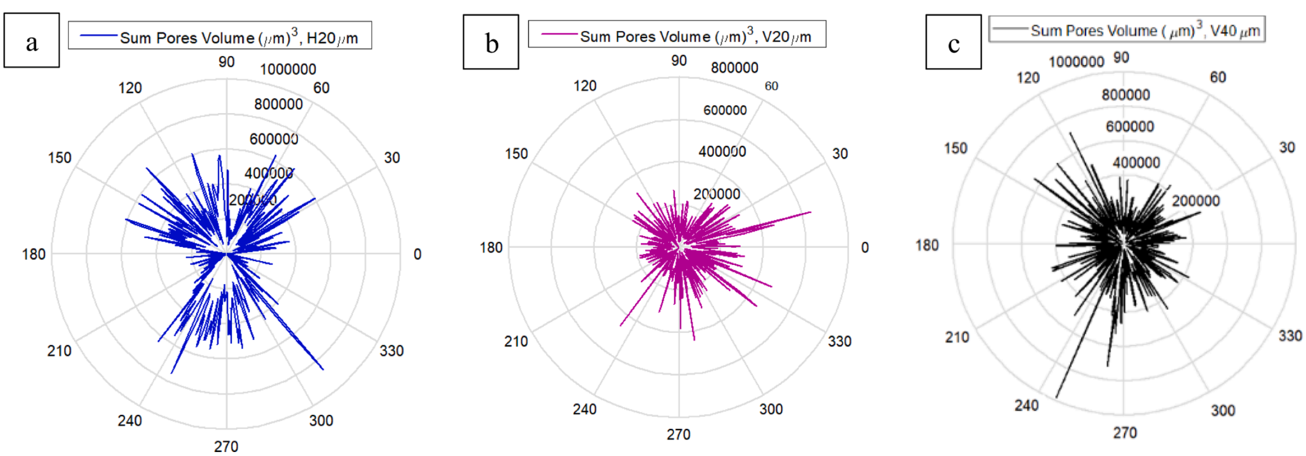

Fig. 8. Comparison of the total volume of pores with respect to the height of the specimen around the specimen axis for (a) horizontal sample with layer thickness 20 μm, (b) vertical sample with layer thickness 20 μm, and (c) vertical sample with layer thickness 40 μm.

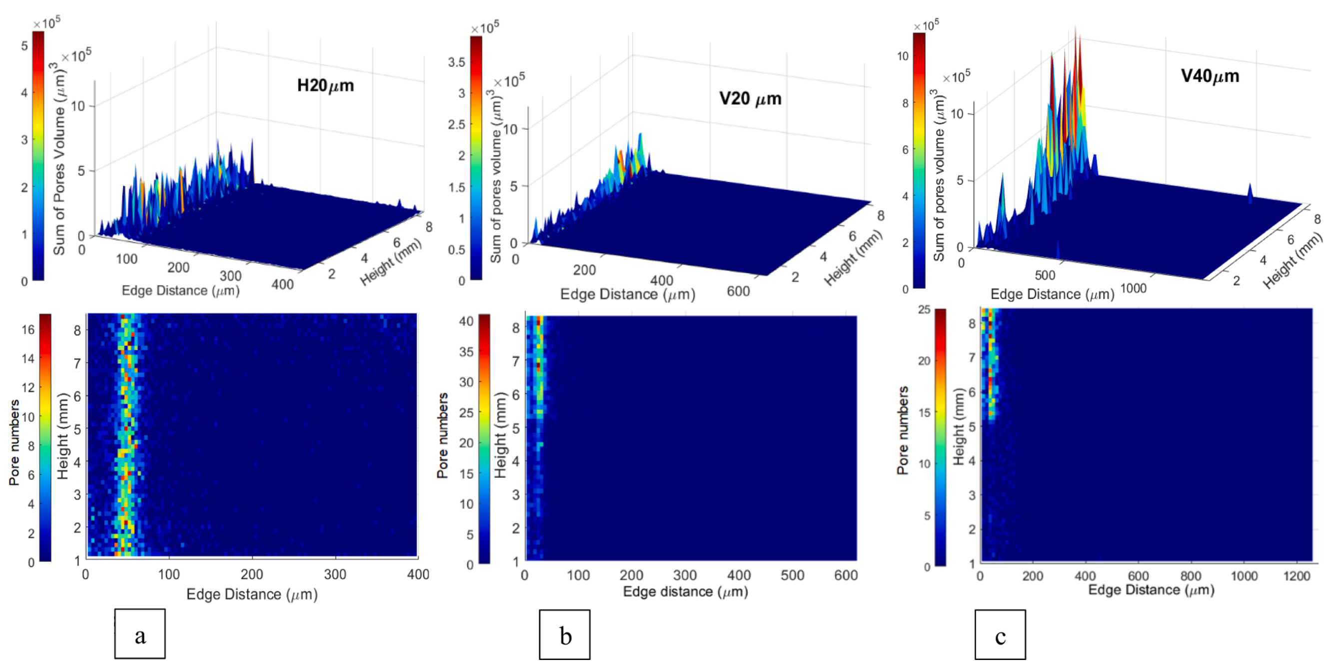

Fig. 9. Pore density map for (a) horizontal sample with a layer of 20 μm, (b) vertical sample with a layer of 20 μm, and (c) vertical sample with a layer of 40 μm.

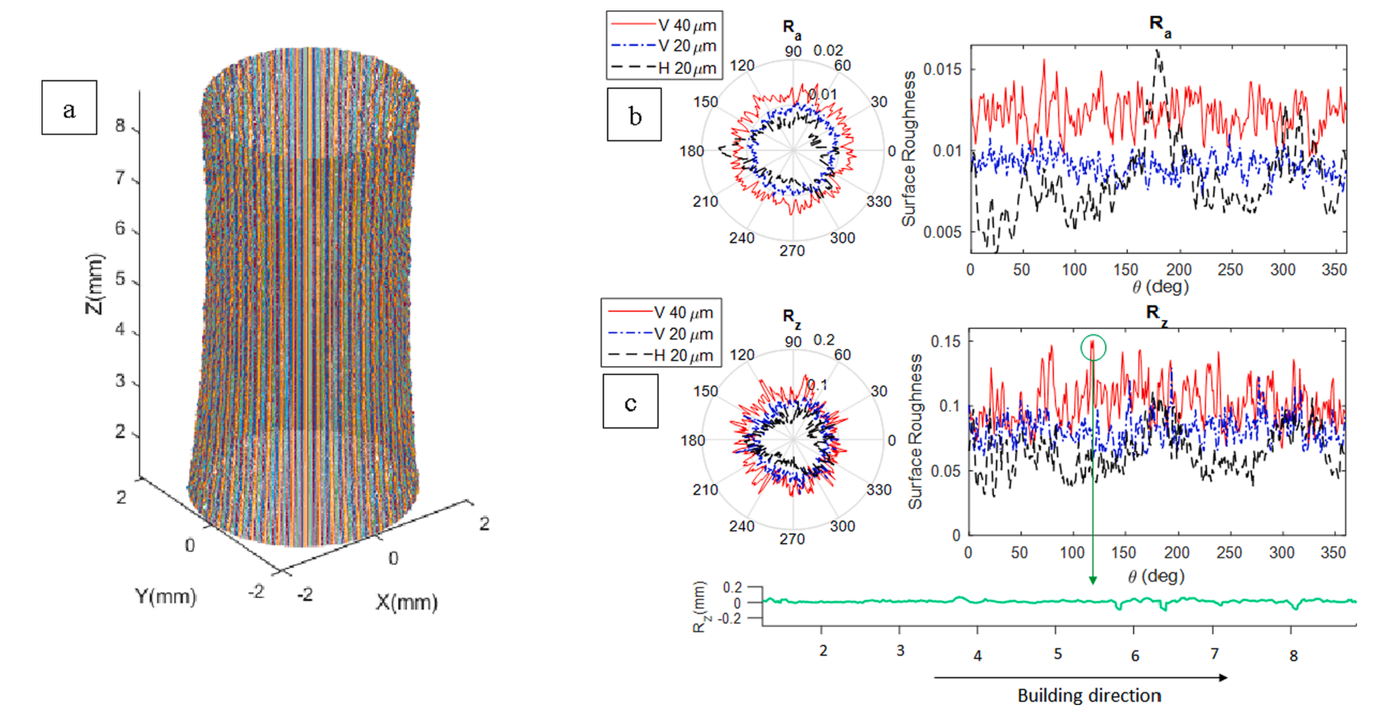

Fig. 10. (a) 3D-sample' surface topologies, (b) the roughness average, R_a, and (c) average maximum height of profile, R_z, distribution around the sample axis with 1° angle interval for vertical specimen with a layer of 40 μm.

force the molten material had the potential to flow against the scanning direction towards a cooler area or a region which was already solidified. This could result in a faster solidification and relatively smaller total melt pool volume leading to concentration of pores one the upper side of the vertical sample. Moreover, sorting powder near the surface due to the tiny vibration of the sample because of the recoater overpass could be a reason for pores concentration on the upper side of the vertical specimen. The probability of sample vibration increases when sample length/width increases. It would be a coincidence that the sample is long enough to vibrate at the pore measurement volume layers.

To predict the size of the largest defects from a 3D defect population, extreme value statistics of defects can be adopted. The extreme value probability distribution of pores' diameter, pores' sphericity, and pores' projected area for different specimens have been shown in Fig. 7a-c, respectively. It has three model types, Gumbel distribution, Frechet distribution, and Weibull distribution. Type I has no upper or lower limits, type II has bounded on the lower end, and type III is bounded on the upper end. Frechet distribution is used in this study to demonstrate maximum values in a data set as it slowly converges to 1. Frechet distribution is equivalent to taking the reciprocal of values from a standard Weibull distribution. The Type II (Frechet) distribution function is as follows [56]:

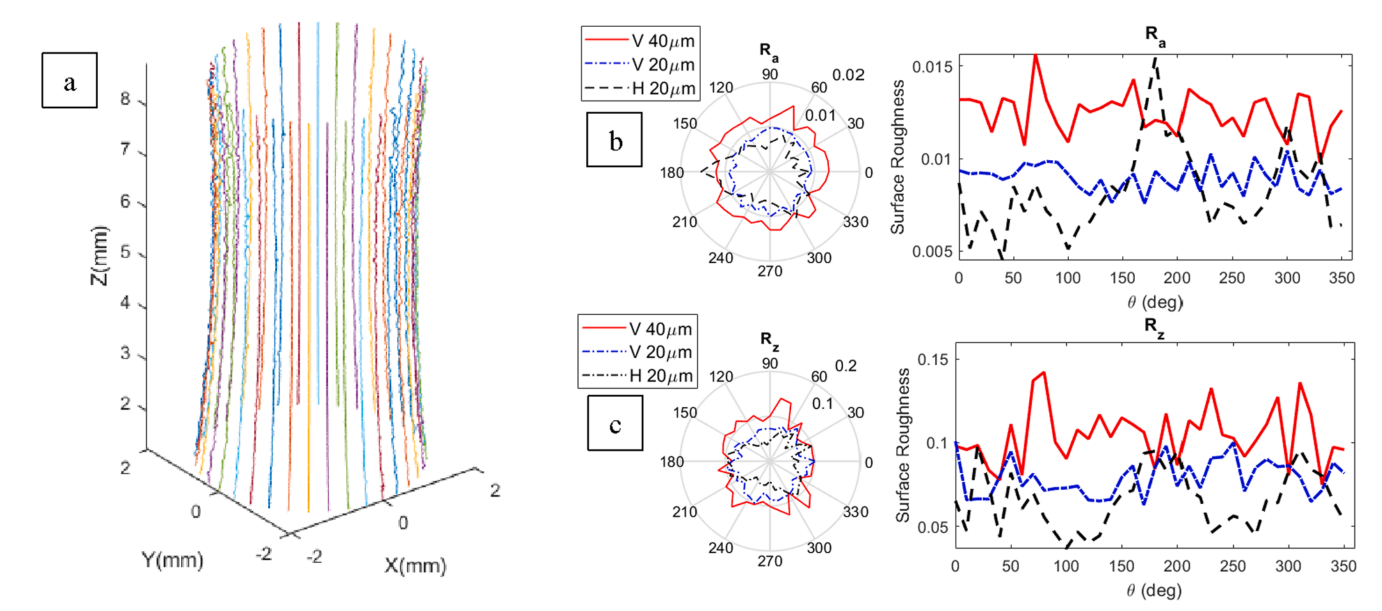

Fig. 11. (a) 3D-sample' surface topologies, (b) the roughness average, R_a, and (c) average maximum height of profile, R_z, distribution around the sample axis with 10° angle interval for vertical specimen with a layer of 40 μm.

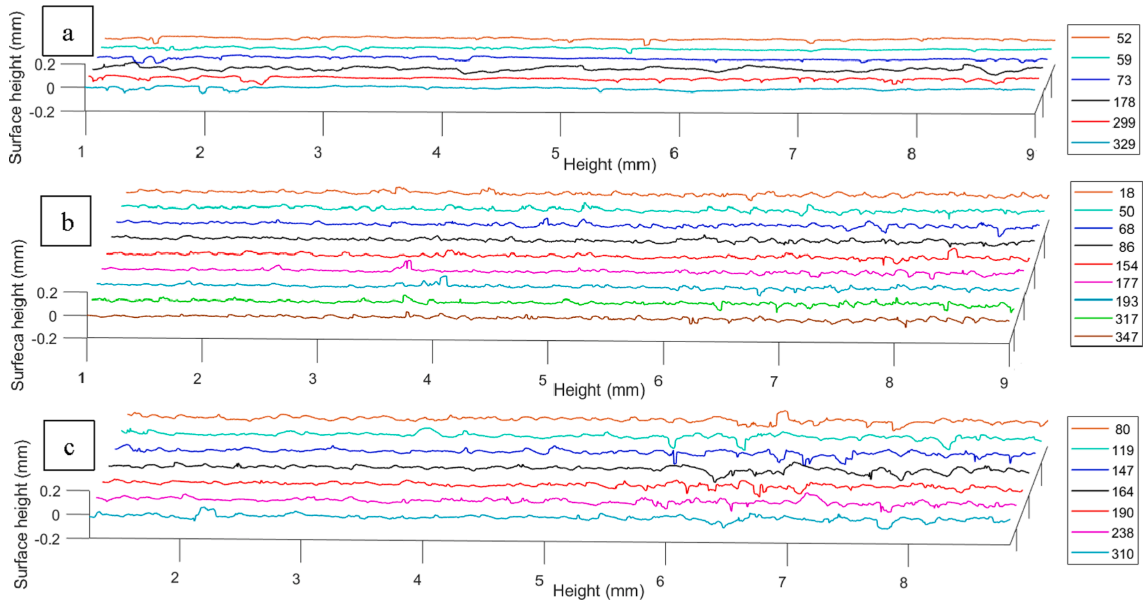

Fig. 12. Critical surface roughness profiles with the biggest R_z values at different angles around the sample axis for (a) horizontal specimen with a layer of 20 μm and (b), (c) vertical specimen with a layer of 20 μm and 40 μm.

$$f(x) = \frac{\alpha}{\beta}\left(\frac{\beta}{x}\right)^{\alpha+1}\exp\left(-\left(\frac{\beta}{x}\right)^{\alpha}\right) \quad (4)$$

where α, β are shape and scale parameters.

Fig. 7a-c depicts that the equivalent defects' diameter and projected area have higher values for vertical samples than the horizontal ones. Moreover, these values are higher for the vertical sample with a higher layer thickness. It can be seen the probability of pores with lower sphericity is higher for the horizontal sample in comparison to the vertical ones. However, the probability distribution is not different for higher sphericity. Moreover, it can be seen that the layer thickness does not seriously affect the probability distribution of sphericity. Thus, sphericity is more sensitive to the building direction than the layer thickness.

Fig. 8a-c shows the total volume of defects with respect to the height of samples around their axis. A clear difference between the vertical and horizontal samples can be observed in this figure. The defects' distribution is not uniform around the specimen axis for vertical samples. As depicted in Figs. 4–6, the defects distribution is also not uniform along the build direction for vertical samples.

Another important factor related to the internal defects' distribution is the distance of pores from the surface of the specimen. This factor can considerably affect the fatigue performance of the samples. The defects closer to the surface create higher stress concentrations than the internal defects far from the surface [57]. Fig. 9a-c depicts pore density maps for vertical and horizontal specimens with different thickness layers. The origin of the plot at zero refers to the exterior surface, and the edge distance demonstrates the radial distance from the exterior surface to the central axis of the specimen. A height dependence with respect to the build orientation is evident in the pore density map for vertical samples, with the greatest density near the top of the specimen. However, this height dependence is not detected in the pore density map of the horizontal specimen. Since the space between surface defects and internal defects as two adjacent defects is important to calculate the effective defect size as introduced in Eq. (3), the edge distance of the pores from the surface is an important parameter.

3.2. Characterization and analysis of surface roughness

Fig. 10a shows the 3D-sample' surface topologies for vertical specimen with a layer of 40 μm using the proposed surface determination algorithm as an example. In this figure, the angle interval showing the surface profiles is 1°. Depending on the needed accuracy, this value can be varied. Fig. 11a depicts the 3D-sample surface topologies with a 10° angle interval for the same sample. The roughness average, R_a, and the average maximum height of profile, R_z, have been calculated for all surface profiles of different samples as depicted in Fig. 10b and 10c with a 1° angle interval. Fig. 10c shows an exemplary surface profile at a specific angle (119°) for the vertical sample with a layer of 40 μm. It is observed that the introduced approach can effectively provide holistic information on the surface topologies of AM parts without any limitations.

Recently, Schneller et al. have studied the effects of as-built surface layers on the fatigue strength of metal AM parts [51]. Representative areal surface texture parameters have been determined using 3D optical topography scans. But, a sharp notch where radii converging zero resulted in limitations as optical capturing and subsequent evaluation might not be acceptable for characterizing the notch geometry. Indeed, the thin and deep defects are systematically overlooked by optical profilometry. Moreover, Persenot et al. have reported the R_a value of as-built Ti-6Al-4 V alloy AM sample based on tomography scans where crack-like notches are detected, is 16% bigger than the average value of R_a obtained by profilometry [58]. Thus, these methods are not suitable for detecting notches, and only X-ray tomography-based roughness measurements might be used for surface roughness characterization and fatigue life prediction. Few studies have utilized this technique; however, they have some limitations due to the lack of a suitable surface roughness determination algorithm for specimens with curved shapes at any angle around the axis [10,59]. The roughness was measured based on tomographic images following the method initially suggested by Suard et al. [10]. A series of surface profiles was extracted from a radial slice every 10° around the cylindrical sample circumference. Thus, 36 profiles have been analyzed for each sample. Persenot et al. have employed the same approach and discussed the shortcoming of the method [58]. This approach can be applied only for cylindrical specimens, and very local surface irregularities such as notch-like defects are thus more probably to be neglected. Figure 10b-c shows R_a and R_z for the vertical sample with a layer of 40 μm with a 10° angle interval. It can be observed the local maximum values in this figure are different from what was detected in Fig. 10b-c, e.g., R_z value at the specific angle, 119°, in Fig. 10b and 10c. This is one of the most critical surface profiles

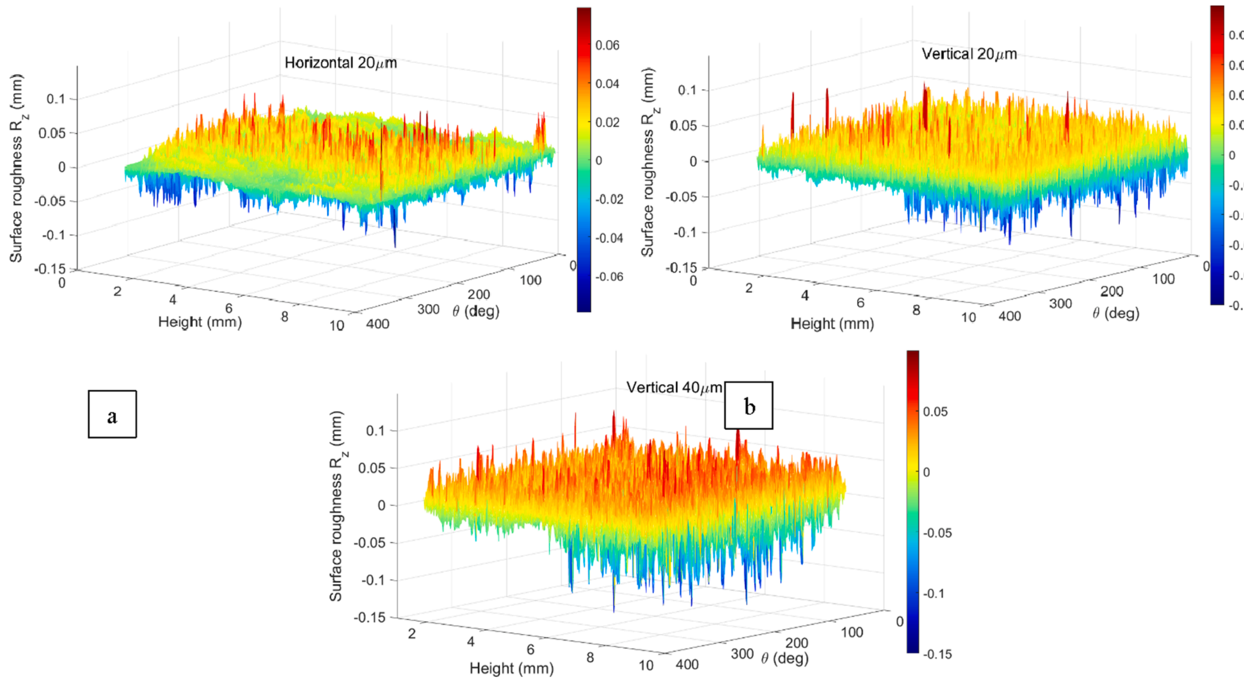

Fig. 13. The roughness of the whole surface around the specimen axis with respect to the height for (a) horizontal specimen with a layer of 20 μm and (b), (c) vertical specimen with a layer of 20 μm and 40 μm.

containing a fatigue origin, see Figs. 16 and 17. However, with 10° angle interval analysis, it has been ignored. The proposed surface roughness characterization approach using the XCT data has comprehensively recognized the local surface irregularities of the dog-bone (curved) shaped sample without any limitations in comparison to the other approaches applied for simple cylindrical shape [38]. It should be noted that the resolution does not allow for roughness measurements near or below the resolution of the scan. The practical limitation for XCT-based surface characterization is the resolution and part size: the voxel size is confined by the part size, and there might be a doubt that this method is suitable for reasonably rough surfaces or small parts. However, this limitation can be handled by determining the critical regions of big parts and carrying out XCT from these specific regions with high enough resolutions.

Using this approach, surface roughness parameters (e.g., R_a and R_z) can be determined for each surface profile around the sample, and the most critical ones can be recognized. In this study, surface profiles with maximum R_z values have been considered as the critical ones. The interaction effect of internal defects and surface roughness at critical locations is important, and R_a cannot be applied to determine this effect. This means that despite the apparent correlation reported in Fig. 10b, 11b, R_a cannot be the relevant parameter for predicting the critical equivalent defect size and fatigue life in the case of as-built AM samples. Fig. 12a-c shows critical surface roughness profiles for samples fabricated with different building directions and layer thicknesses. Five to ten surface profiles of different samples with the biggest R_z values are depicted in this figure as critical surface profiles for each sample. It can be seen the surface roughness values are bigger for the vertical sample with a thicker layer (40 μm) in comparison to the horizontal sample or the vertical one with a thinner layer (20 μm). Fig. 13a-c shows the roughness of the whole surface around the specimen axis with respect to the height of samples with different building directions and layer thicknesses. A homogeneously distributed roughness profile is observed for the horizontal sample. In contrast, the roughness profile distribution is not homogeneous for vertical samples, and the maximum pit depth is concentrated on the upper side of the specimen along the build direction. These results indicate the roughness profile distribution depends on the building direction and the layer thickness parameter. As the building inclination increases from 0° in the horizontal sample to 90° in the vertical one, surfaces get more complex along the height of the specimen. Moreover, the surface roughness of the thinner layer tends to be better than that of the thicker ones.

The reduced layer thickness led to decreased gaps and consequently less geometric inaccuracy. This has resulted in decreased areal notch valley depth values, as shown in Fig. 12a-c and 13a-c. Previous studies have found that a small layer thickness ensures finer particle sizes and facilitates a more complete melting process due to the higher surface-to-volume ratio than a larger layer thickness [60,61].

It should be noted the obtained results in sections 3.1 and 3.2 may explain the correlation between defects (internal and surface) characteristics and the anisotropic fatigue performance of metal AM parts, as indicated in Fig. 3. Indeed, the thermal history experienced by parts fabricated in different build orientations is not necessarily identical. And this can result in anisotropic characteristics of defects and microstructure, leading to anisotropic fatigue resistance of metal AM materials [62,63].The anisotropic characteristics of the internal defects' population and surface defects as non-homogeneous roughness profile distribution of metal AM parts have been investigated using the proposed characterization approach. However, further study is still required to investigate the combined effects of anisotropic defects (internal and surface) and microstructure characteristics on the fatigue performance of metal AM material. This information can thoroughly describe the anisotropic fatigue damage mechanism in metal AM materials.

3.3. Critical equivalent defect size using 3D pores and surface roughness characterization

Using the proposed characterization approach for internal and surface defects, it is possible to calculate the critical equivalent defect size as introduced in Eq. (3). For this purpose, first, the XCT data has been analyzed using the proposed surface roughness characterization approach, and 5–10 critical surface profiles with the biggest R_z values at different angles around the sample axis have been detected. Then, these critical surface profiles have been separately checked to find the deepest valleys (R_v). At the corresponding height of the deepest valleys along the sample, the presence of the internal defect, its projected area ($\sqrt{area_D}$),

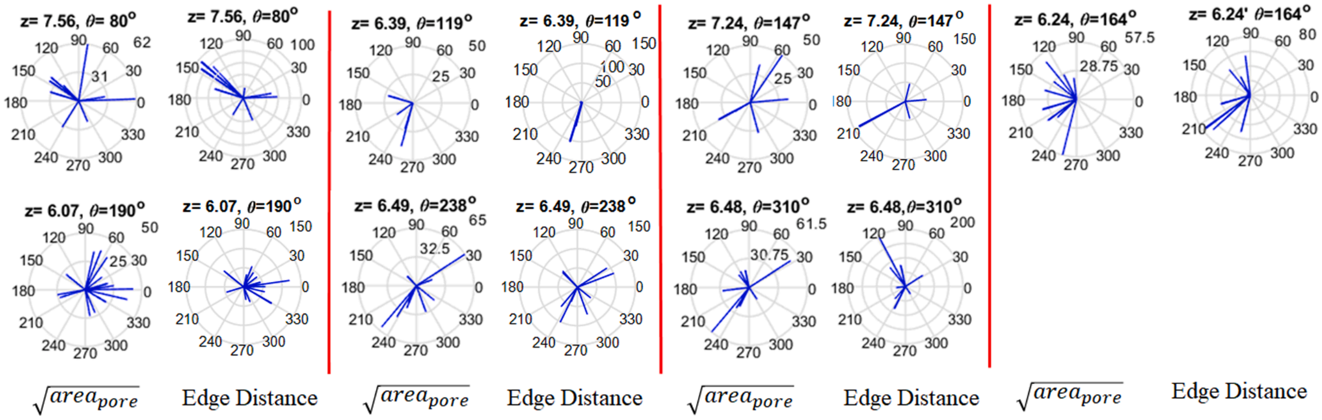

Fig. 14. Polar distribution of projected internal defects' areas ($\sqrt{area_D}$), and their distances from the edge, (d_{R-D}), at the specific height of the sample related to the deepest valleys on critical surface profiles for the vertical sample with a layer of 40 µm.

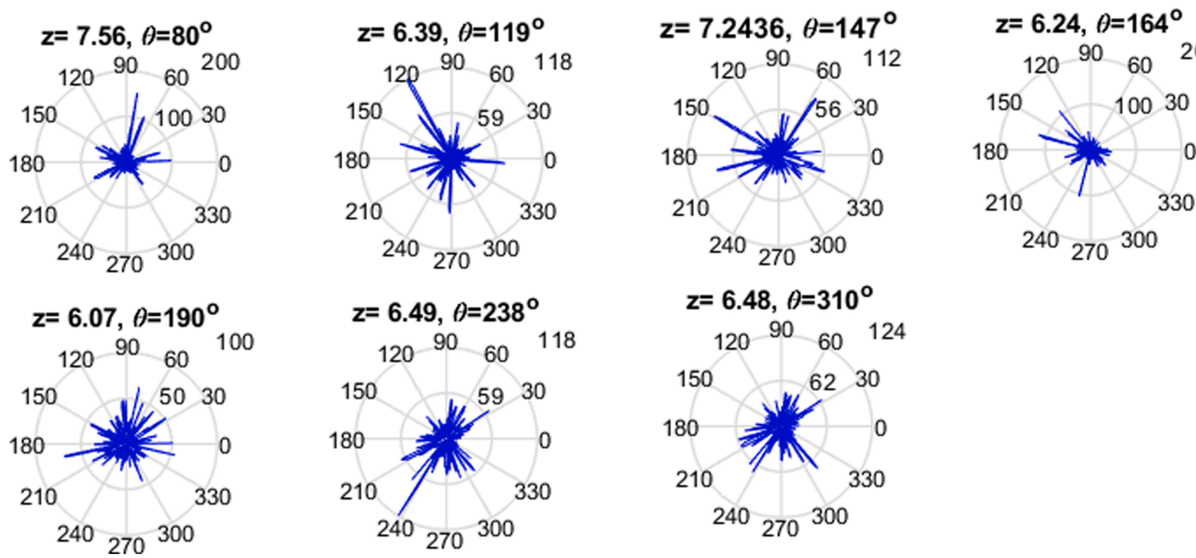

Fig. 15. Polar distribution of the critical equivalent defect at the specific height of the sample related to the deepest valleys on critical surface profiles for the vertical sample with a layer of 40 µm.

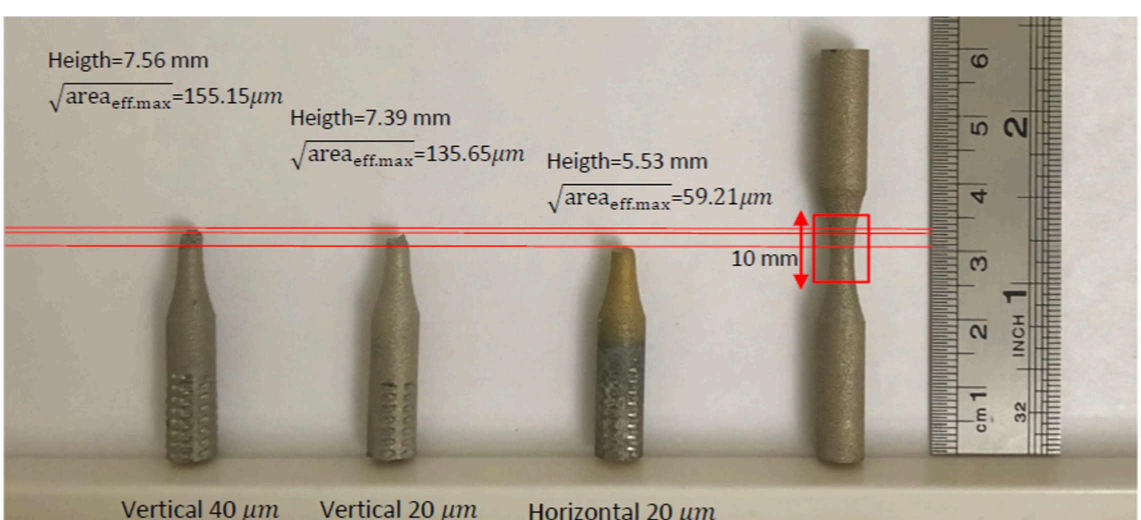

Fig. 16. Schematics of different specimens (horizontal with a layer of 20 µm and vertical with a layer of 20 µm and 40 µm) fractures at different heights.

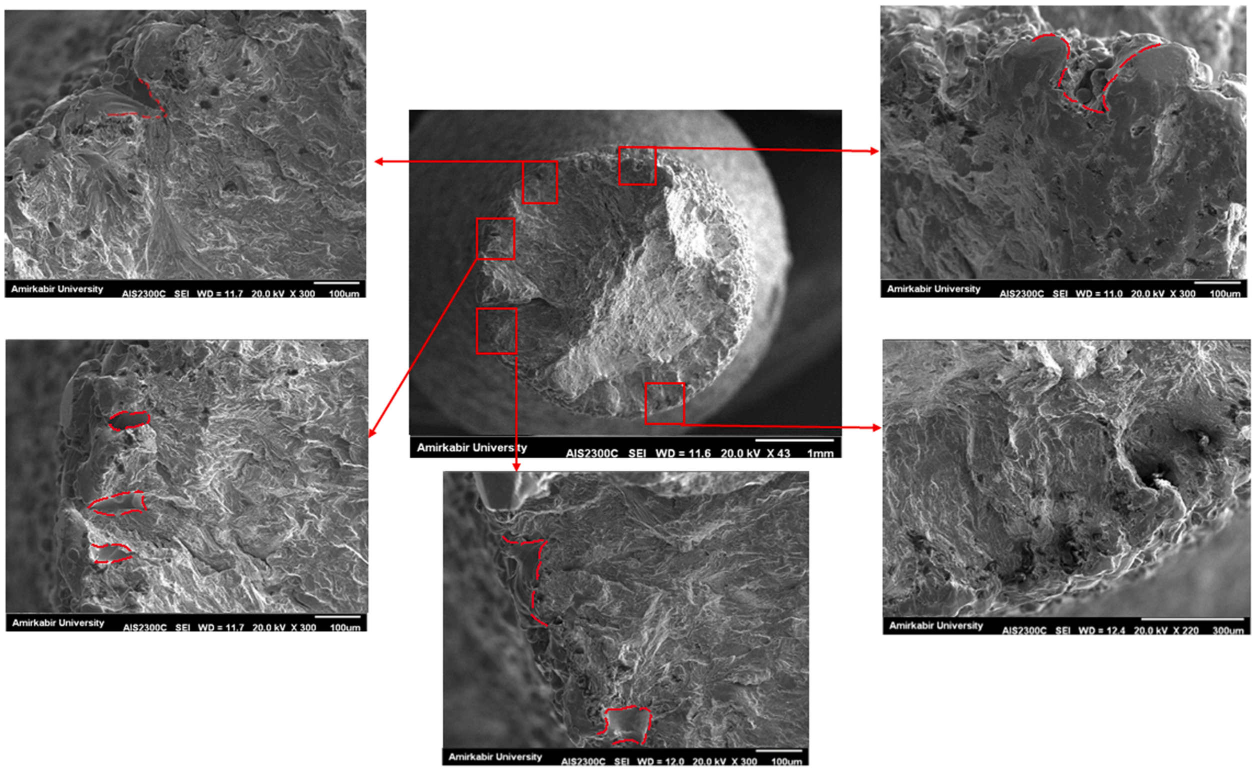

Fig. 17. SEM top views of the fracture surfaces of the vertical sample with a layer of 40 µm that failed due to volumetric defects and surface features. Sample tested at stress amplitude of 170 MPa. Higher magnification images showing the crack initiation sites.

Table 1
The critical equivalent defect at the specific height of the sample related to the deepest valleys on critical surface profiles around the sample axis for the vertical specimen with a layer of 40 µm.

θ(deg)	Height(z)(mm)	R_v(µm)	$\sqrt{area_D}$ + d_{R-D}(µm)	$\sqrt{area_{eff.max}}$(µm)
80	7.56	75.1538	80	155.1538 (Maximum value)
119	6.39	112.538	0	112.538
147	7.24	84.3455	0	84.3455
164	6.24	105.151	38	143.151
190	6.07	65.594	23.5	89.094
238	6.49	74.0119	43.5	117.5119
310	6.48	75.1741	14.4	89.5741

Table 2
The critical equivalent defect at the specific height of the sample related to the deepest valleys on critical surface profiles around the sample axis for the vertical specimen with a layer of 20 µm.

θ(deg)	Height(z)(mm)	R_v(µm)	$\sqrt{area_D}$ + d_{R-D}(µm)	$\sqrt{area_{eff.max}}$(µm)
18	5.62	60.1603	0	60.1603
50	7.39	73.6546	62	135.6546 (Maximum value)
68	7.88	88.2481	0	88.2481
86	7.56	53.7007	36	89.7007
154	6.95	74.3783	34	108.3783
177	7.42	56.1794	18.7	74.8794
193	5.95	73.5126	25	98.5126
317	6.14	79.2052	0	79.2052
347	7.32	71.0451	0	71.0451

and its distance from the edge or deep valley as a surface defect (d_{R-D}) have been determined. If d_{R-D} is smaller than the size of the smaller defect ($\sqrt{area_D}$ or R_v), the space between these two defects has been considered in the calculation of the critical equivalent defect size. Otherwise, only the larger defect was taken into account in the fatigue limit prediction process. Thus, the interaction effect of both internal and surface defects has been considered using the introduced approach. Moreover, the surface defects size has been calculated without any limitation in catching some critical features of surface profiles as discussed in Refs [49,51]. Besides overcoming this limitation and considering the internal and surface defects interaction in calculating the critical equivalent defect size, the proposed approach can effectively predict fatigue failures' critical locations before testing at specific angles around the sample axis and heights along the sample. The proposed defects determination algorithm, including characterization of internal and surface defects, has overcome the limitations of the previous studies. Fig. 14 shows the polar distribution of projected internal defects' areas ($\sqrt{area_D}$) and their distances from the edge, (d_{R-D}), at the specific height of the sample that the deepest valleys have been recognized using surface roughness characterization for the vertical sample with a layer of 40 µm. In the next step, distances of the projected areas from the surface defects (valleys) have been checked whether they are smaller than the smaller defects or not, and the critical values, $\sqrt{area_D} + d_{R-D}$, have been calculated. Then, the deepest valley value, R_v, has been added to these critical values as proposed in Eq. (3) to calculate the critical equivalent

Table 3
The critical equivalent defect at the specific height of the sample related to the deepest valleys on critical surface profiles around the sample axis for the horizontal specimen with a layer of 20 µm.

θ(deg)	Height(z)(mm)	R_v(µm)	$\sqrt{area_D}$ + d_{R-D}(µm)	$\sqrt{area_{eff.max}}$(µm)
52	5.53	59.2134	0	59.2134 (Maximum value)
59	5.45	44.4948	0	44.4948
73	6.20	26.9116	0	26.9116
178	4.12	10	0	10
299	5.79	36.8841	0	36.8841
329	5.34	24.8288	0	24.8288

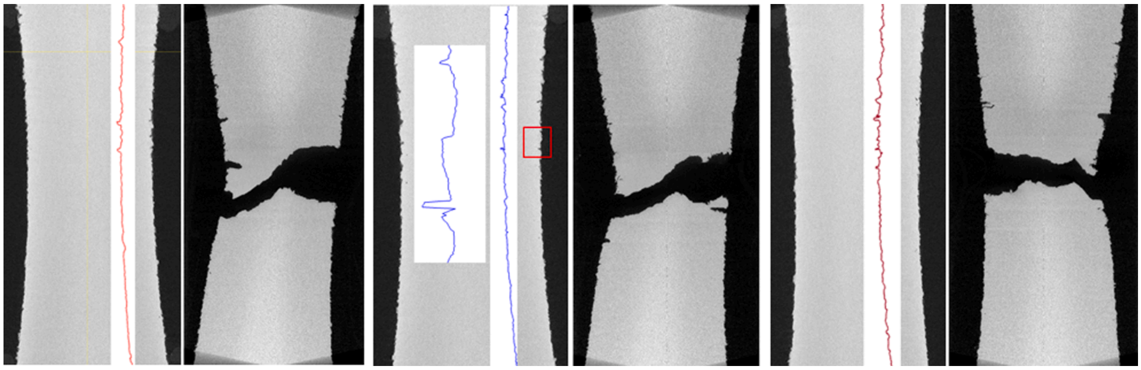

Fig. 18. Radial slices obtained by X-ray tomography of a sample before and after fatigue failure at specific angles as exemplary cases from the critical surface profiles.

defect size, $\sqrt{area_{eff}}$. Fig. 15 depicts the polar distribution of the critical equivalent defect at specific heights of the sample based on the location of the deepest valleys in the critical surface profile for the vertical sample with a layer of 40 μm. This figure demonstrates that the most critical defect at the specific height around the sample axis takes place at the predicted location. Thus, $\sqrt{area_{eff}}$ can effectively represent the critical equivalent defect. Table 1 presents the value and location (specific angle round the sample axis and specific height along the sample) of the critical equivalent defects for the vertical sample with a layer of 40 μm based on the proposed method. The same approach has been applied for XCT data of intact vertical and horizontal samples with a layer of 20 μm. Results have been presented in Table 2 and Table 3, respectively. Results predict before the fatigue testing that fatigue failures will originate from several locations with respect to the height of the sample around its axis. Table 1 and Table 2 foresee that fatigue failures in vertical samples may cause by both volumetric defects and surface-related features; however, Table 3 does not predict any volumetric defects for the horizontal sample. Volumetric defects present the interaction effect between surface and internal defects. The next section will validate the results using fracture surface analysis for different samples.

It should be noted although R_z has a big value for the surface profile of the horizontal sample at 178° as depicted in Fig. 10c, this profile does not contain any deep valley as a critical location along the sample for fatigue failure, as presented in Table 3. The big value of R_z for this surface profile is related to the higher peak values at this profile and not due to the deep valleys, as shown in Fig. 12a. Thus, it is not appropriate to only consider the surface roughness effect in fatigue performance of metal AM specimen using R_z or R_a value as presented in Ref. [11]. The proposed approach in this study precisely checks the surface roughness effect on the fatigue life of metal AM parts and predicts the potential sites for fatigue failure. It can be seen that these predicted potential sites correlated to $\sqrt{\mathrm{area}_{\mathrm{eff.max}}}$, as presented in Tables 1, 2, and 3, are located at different heights which are not in the middle of the sample where theoretically, the stress is the maximum. Experiments illustrate that samples have been fractured with good agreement at the predicted height corresponding to the maximum $\sqrt{\mathrm{area}_{\mathrm{eff.max}}}$, as shown in Fig. 16. Therefore, the stress amplitude of the specimen can be recomputed, according to the cross-sectional area at these height. Chen et al. [64] have recently proposed to substitute the local stress for the net loading stress, to investigate the effect of metallurgical defects and stress levels on high cycle fatigue properties using stress recalculation according to the cross-sectional area of the fracture head.

3.4. Fracture surface analysis

To identify the failure mechanisms, the fracture surfaces of samples with different build orientations and layer thickness have been systematically examined by SEM. As said earlier, all detailed studied

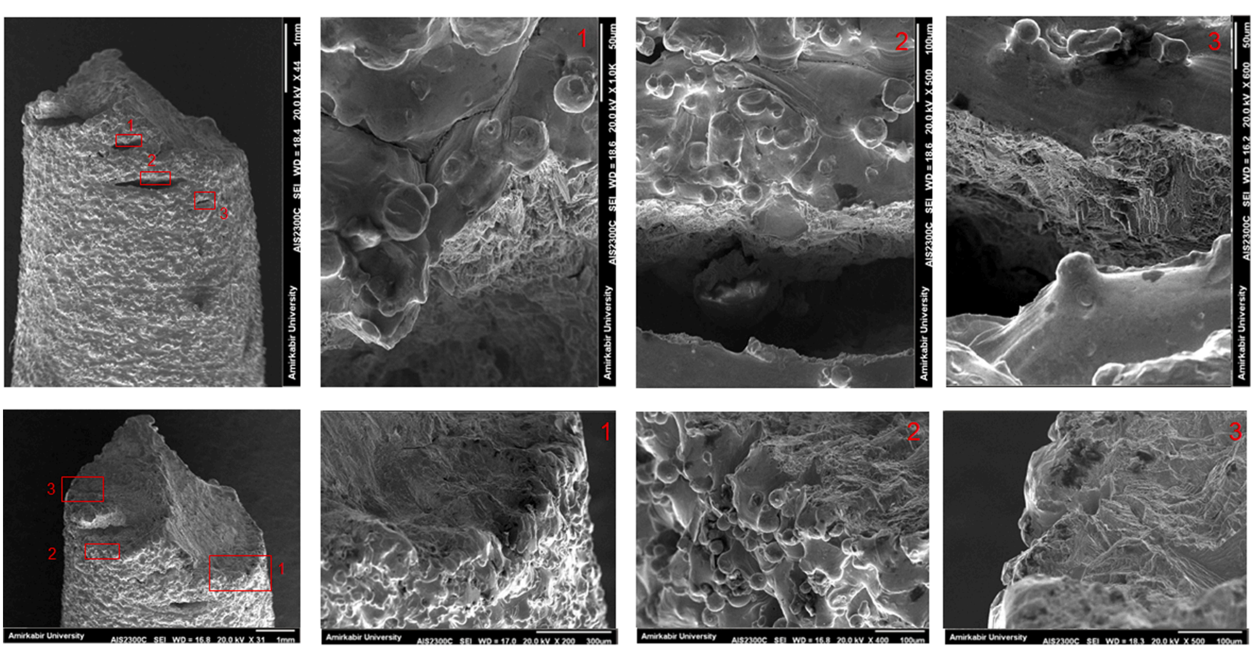

Fig. 19. Fractography of the vertical sample with a layer of 40 μm, (a) front view of the damage locations on the surface, and (b) front view of the fatigue origins.

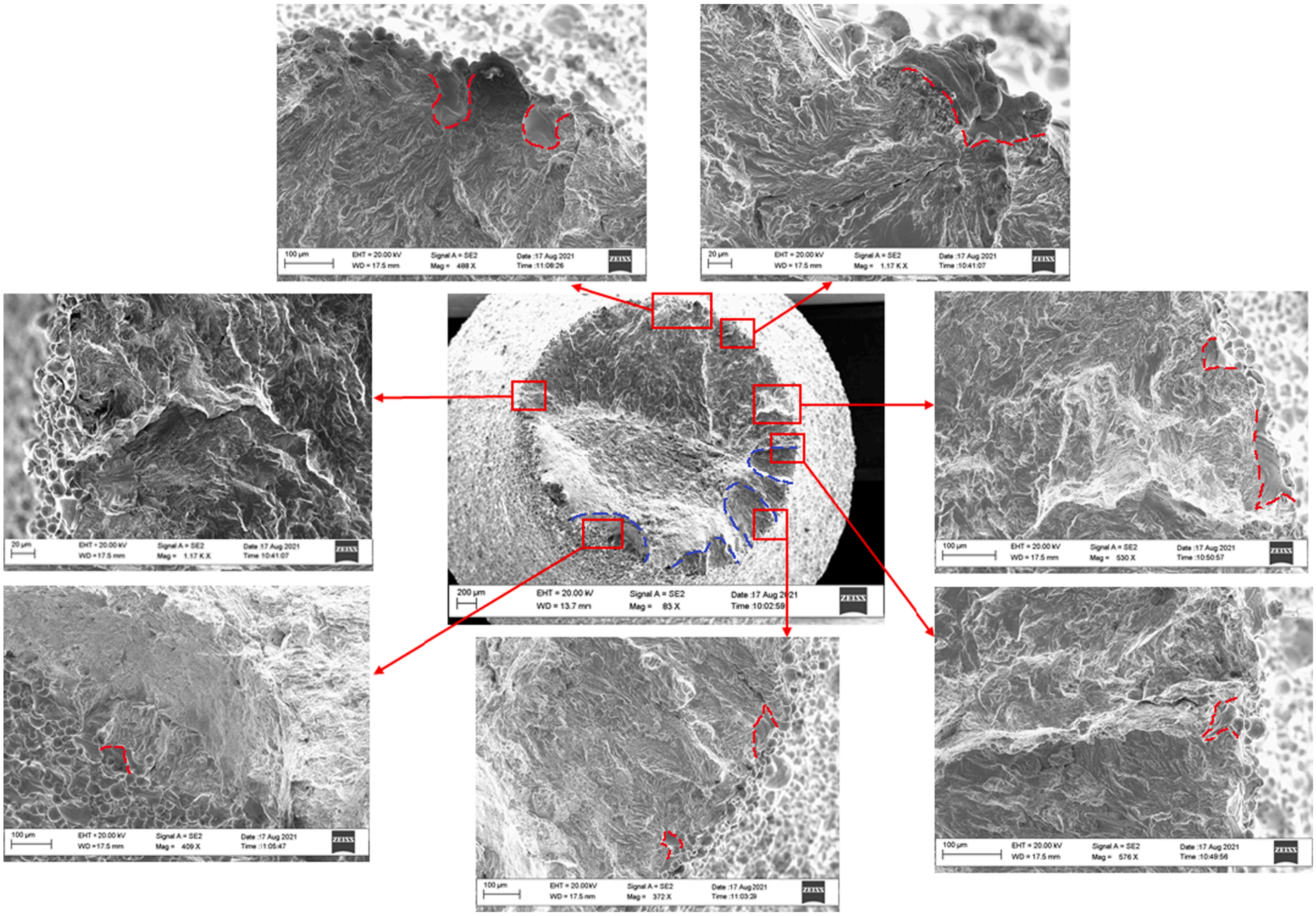

Fig. 20. SEM views of the fracture surfaces of the vertical sample with a layer of 20 μm. Sample tested at stress amplitude of 170 MPa. Higher magnification images showing fatigue origins.

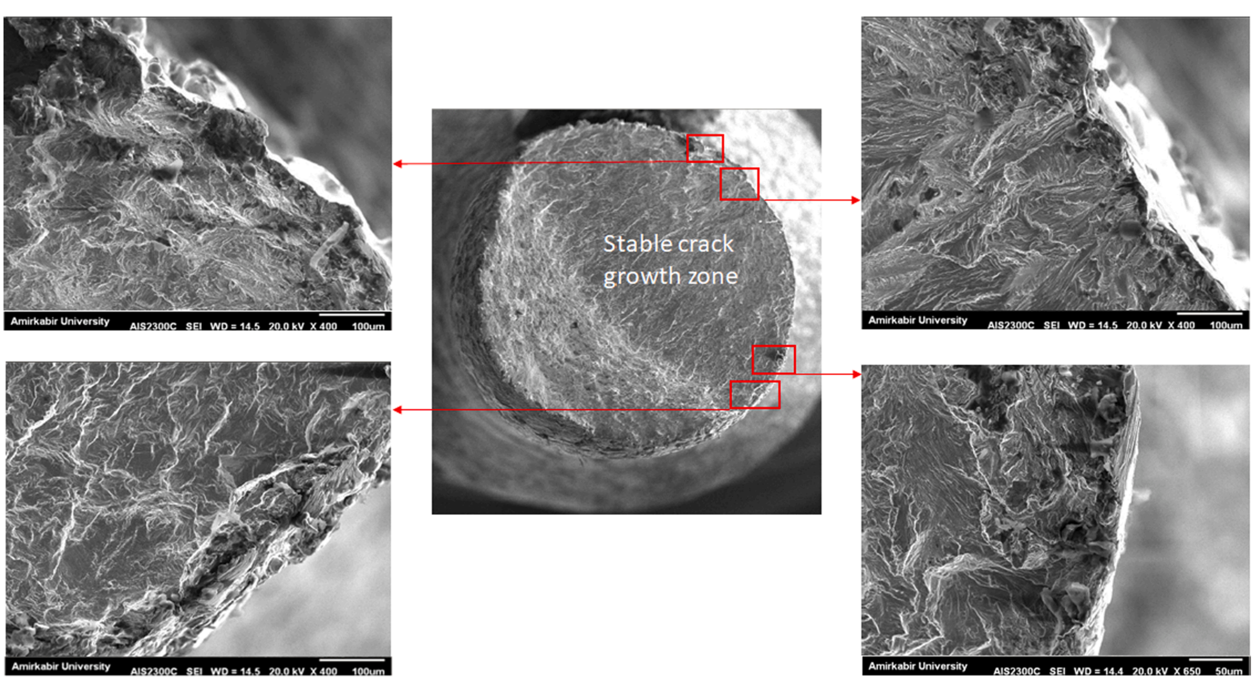

Fig. 21. SEM views of the fracture surfaces of the horizontal sample with a layer of 20 μm. Sample tested at stress amplitude of 170 MPa. Higher magnification images showing fatigue origins.

Table 4
Comparison of the predicted and experimental fatigue limits for different samples.

Sample	$\sigma_{wl,exp}/\sigma_{wl,pred}$
Horizontal, 20 µm	0.84
Vertical, 20 µm	0.7
Vertical, 40 µm	0.56

samples have been tested at the same stress amplitude with a nominal stress range of 170 MPa, and then fractographic analyses of SEM images have been carried out. Fig. 16 shows the fracture surface of the vertical sample with a layer of 40 µm at stress amplitude 170 MPa. Post-mortem fractographic analyses of SEM images depict the nucleation sites and extent of the crack growth region. It can be observed that cracks initiate at many locations on the surface in the presence of high surface roughness and volumetric defects. The fatigue origins have been located at almost the same angles that the proposed surface characterization approach predicts critical surface profiles as potential sites for crack initiation using XCT data from the sample before fatigue testing, see Fig. 10c. Moreover, it can be seen fatigue origins are mainly located on the side that the overall concentration of internal pores is higher, see Fig. 8c. In this sample, the failures were caused by volumetric defects and surface-related features (Fig. 17) with almost equal probability. Fig. 18a-c depicts three radial slices obtained by X-ray tomography of a sample before and after fatigue failure at specific angles. These angles have been selected as exemplary cases from the critical surface profiles, see Fig. 12c. It can be seen on each critical surface profile there might be several deep valleys at different heights.

One of the most important advantages of the proposed characterization approach for defects and surface topographies is the possibility to predict the fatigue origins at different locations around the sample (at specified heights and angles). Using this approach, it is possible by performing a CT scan before the fatigue testing to predict from which defect of the thousands detected the failure would originate. The obtained results using the proposed determination defects algorithm employed for XCT data before the fatigue testing in section 3.3 indicate there would be several critical locations for fatigue failure around the sample's axis at different heights. These results have been validated with experiments as depicted in Fig. 17 and Fig. 19a-b. Besides the top view of the fractures surface (Fig. 17), Fig. 19a-b shows the front view of the fractured vertical sample with a layer of 40 µm. The fatigue origins have been located at different heights around the sample axis (different angles), as predicted in Table 1 before fatigue testing. The higher magnification of these locations is depicted in Fig. 19b. Moreover, it can be observed there are other critical sites on the surface of the specimen in which damage initiated from surface irregularities (Fig. 19a-1, Fig. 19a-3) or the volumetric defect (Fig. 19a-2). It can be seen there is a good correlation between the predicted results and the experiment. Figs. 20 and 21 depict the fracture surfaces of the horizontal and vertical sample with a layer of 20 µm. In the horizontal sample, the crack leading to failure initiates from a surface defect. However, in the vertical sample, the failures were caused by both volumetric defects and surface-related features. The relatively large flat zone corresponding to the stable crack propagation regime can be observed for the horizontal sample. The size of the stable crack growth zone, $area_{st}$, scales with the fatigue lives ($area_{st}|_{vertical} < area_{st}|_{horizontal}$). It is worth mentioning the comparison between Table 2 and Fig. 20 and Table 3 and Fig. 21 demonstrates the accuracy of the proposed approach to predict fatigue origins before fatigue testing.

3.5. Effect of defect size on fatigue life

The lower bound of the fatigue limit, σ_{wl}, can be determined by the defect size parameter ($\sqrt{area}$) as introduced in Eq. (1). Using the proposed defect characterization approach, this parameter can be replaced with $\sqrt{area_{eff,max}}$ for fatigue limit prediction. The maximum critical effective defect size value has been obtained from Table 1, Table 2, and Table 3 for different samples. Table 4 shows the fatigue limits normalized by prediction values for vertical and horizontal samples with different layers of thicknesses. As demonstrated in this table, the fatigue limit of the horizontal sample with a layer of 20 µm is in good agreement with the prediction by the $\sqrt{area_{eff,max}}$ parameter model (i.e., $\frac{\sigma_{wl,exp}}{\sigma_{wl,Pred}} = 0.84$). However, the fatigue limit of vertical samples with larger defect sizes is well below the predicted ones.

This phenomenon can be explained as follows. First, it should be noted that the fracture mechanics-based $\sqrt{area}$ model is applicable to

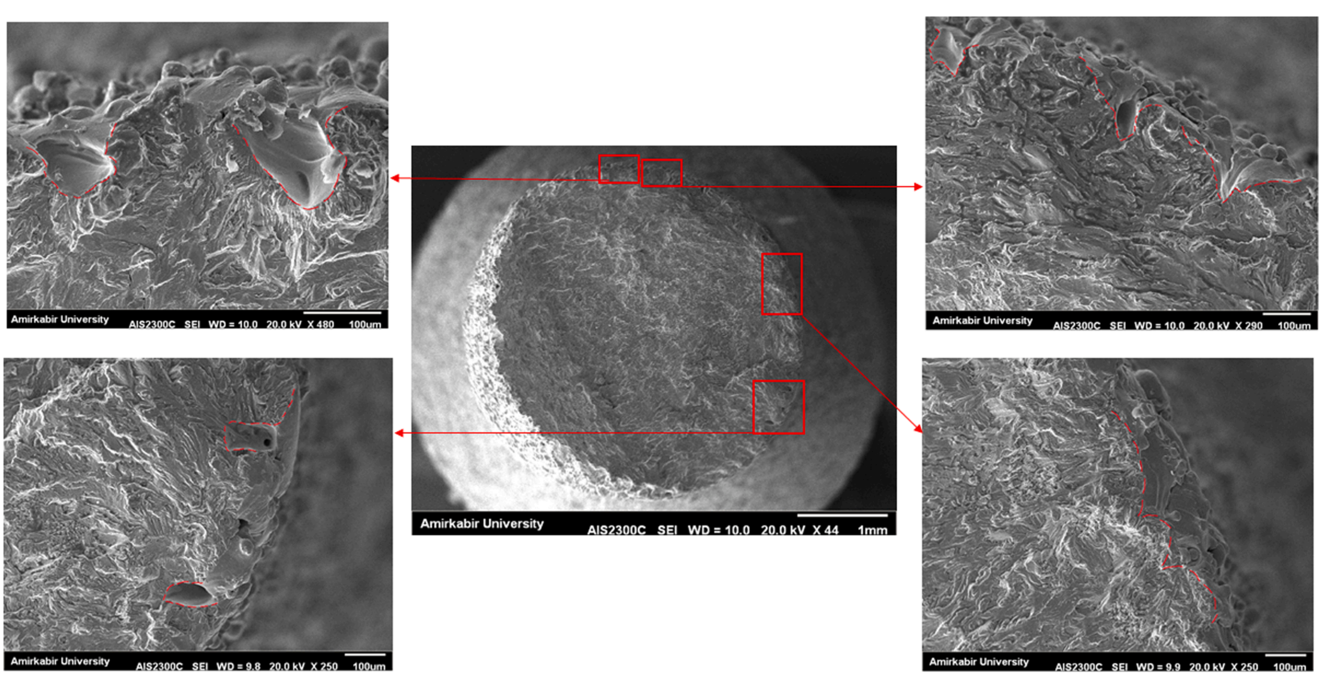

Fig. 22. Δk_{th} and determination of transition point of $\sqrt{area}$ for small and long crack.

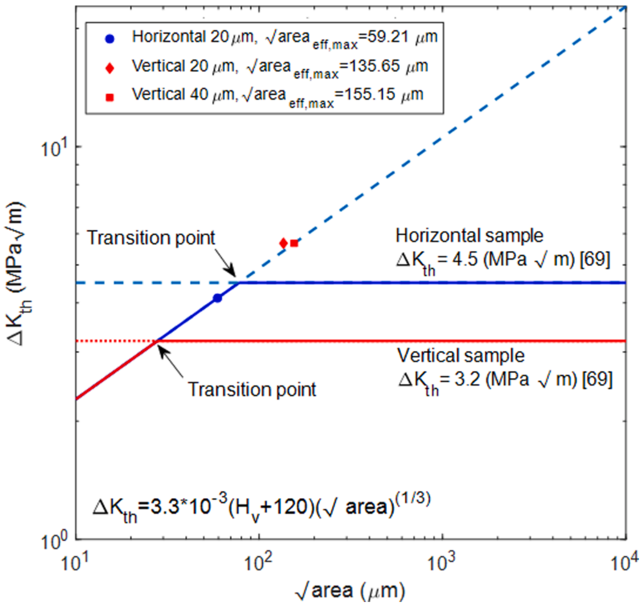

Fig. 23. SEM top views of the fracture surfaces of the vertical sample with a layer of 40 μm. Sample tested at stress of 85.5 MPa (N_f = 1396166).

the small crack, but not to the large crack, and it is important to check the small/large crack-transition size [65,66]. The crack-transition size for different samples has been determined using Δk_{th} as depicted in Fig. 22. The threshold value has been used from Ref [67] corresponding to the studied material. It can be seen that the maximum critical effective defect size for horizontal sample ($\sqrt{area_{eff,max}} = 59.2\,\mu m$, see Table 3) is in the region that small crack and linear elastic fracture mechanics conditions hold; thus $\sqrt{area}$ parameter model can be applied, and the result is in good agreement with the experiment. However, $\sqrt{area_{eff,max}}$ values for vertical samples and the corresponding Δk_{th} are bigger than the transition point of $\sqrt{area}$ and crack growth threshold value for non– propagative crack growth region. Therefore, this model overestimates the fatigue limit of these samples in comparison to experiments. Second, the higher surface roughness of as-built vertical samples and surface and internal defects interaction result in a multi-origins fatigue failure mechanism as predicted using the proposed characterization approach and confirmed by fractography (see Figs. 17 and 20). The synergic deteriorative influence of these different imperfections may affect these specimens' fatigue life and overestimate their fatigue limit. Figs. 23 and 24 depict the fracture surfaces of the horizontal sample with a layer of 20 μm and vertical sample with a layer of 40 μm in the high cycle region at stress amplitude, 157.5 MPa, and 85.5 MPa, respectively. In Fig. 23, it can be seen the surface and internal defects interaction at different locations around the sample and the multi-origins fatigue failure mechanism are active in the high cycle region for the vertical sample. However, this mechanism cannot be observed for the horizontal sample (see Fig. 24).

Results indicate that defects with larger sizes (the surface roughness of as-built specimen and its interaction with internal defects) cannot be considered small crack-like defects anymore, highlighting the importance of checking the applicability limit of the $\sqrt{area}$ parameter model before its application to AM defects. Instead, the large defect should be considered as a long crack or notch, depending on the defect shape. However, further studies are still required to find the best solution and thus this topic is left as future work.

4. Conclusions

This paper has proposed an innovative approach to characterize metal AM components' complex defects and surface topologies using XCT. Variability in defect characteristics, including size/volume, sphericity, location (distance from the surface), and surface roughness irregularities, has been investigated using the proposed approach to evaluate and quantify their effects on the fatigue performance of these materials. Furthermore, the impact of different processing strategies (layer thicknesses and built directions) on the fatigue performance of stainless steel 316L specimens has been investigated using the proposed method. The main findings of this study can be concluded as follows:

The fatigue performance of specimens fabricated horizontally is

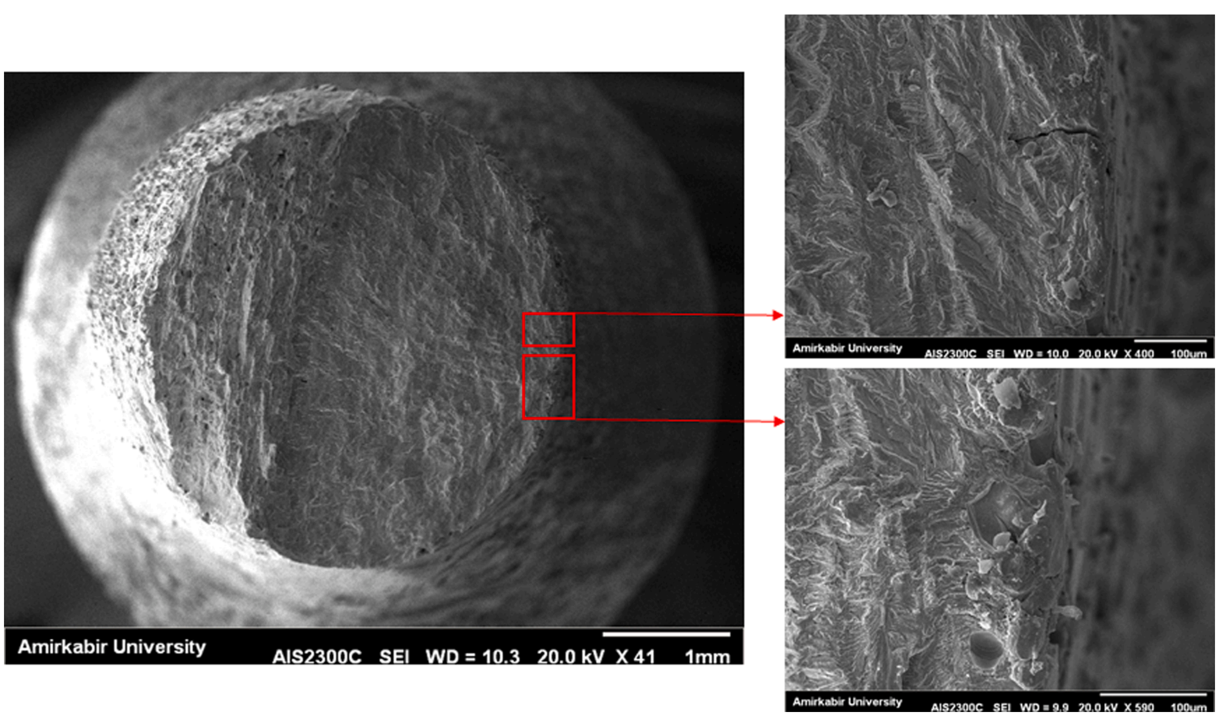

Fig. 24. SEM top views of the fracture surfaces of the horizontal sample with a layer of 20 μm. Sample tested at stress of 157.5 MPa (N_f = 864631).

higher than those fabricated vertically with different thicknesses of layers due to various internal defect sizes and surface roughness. 3D (internal and surface) defects analysis provides effectively further information about the reasons for these differences.

Internal defect characterization cannot include all detrimental features on the fatigue strength of the metal AM parts. Surface defects are more harmful to fatigue life than internal ones. The interaction effect of internal defects and surface roughness is essential, and therefore, the defects' proximity to the surface is necessary and should be studied.

The proposed surface determination algorithm applied for XCT data overcomes the limitations of previous methods and can effectively provide holistic information on the surface topologies of metal AM components. Using this approach, the surface roughness parameters can be determined for all surface roughness profiles around the sample, and the most critical one can be recognized.

The most crucial advantage of the proposed characterization approach for defects and surface topographies is the possibility to predict the fatigue origins at different locations around the sample axis (at specified heights and angles). Using this approach, it is possible by performing a CT scan before the fatigue testing to predict from which defect of the thousands detected the failure would originate.

The defect-based life prediction method cannot deal with all cases where surface defects and their interaction with internal defects lead to the larger equivalent defect size. Therefore, the concept of small defects should be considered in $\sqrt{area}$ parameter model.

- The obtained results in this study can lay a basis for considering how the processing parameters can be optimized to maximize the fatigue life for a given loading cycle.

Declaration of Competing Interest

The authors declare that they have no known competing financial interests or personal relationships that could have appeared to influence the work reported in this paper.

References

[1] Cooke S, Ahmadi K, Willerth S, Herring R. J Manuf Process 2020;57:978–1003. https://doi.org/10.1016/j.jmapro.2020.07.025.
[2] Blakey-Milner B, Gradl P, Snedden G, Brooks M, Pitot J, Lopez E, et al. Mater Des 209 2021:110008. https://doi.org/10.1016/j.matdes.2021.110008.
[3] Khodabakhshia F, Farshidianfarb MH, Gerlichc AP, Noskod M, Trembosovad V, Khajepourc A. Addit Manuf 2020;31:100915. https://doi.org/10.1016/j.addma.2019.100915.
[4] Seifi M, Gorelik M, Waller J, Hrabe N, Shamsaei N, Daniewicz S, et al. JOM 2017;69(3):439–55. https://doi.org/10.1007/s11837-017-2265-2.
[5] Yadollahi A, Shamsaei N. Int J Fatigue 2017;98:14–31. https://doi.org/10.1016/j.ijfatigue.2017.01.001.
[6] Frazier WE. J Mater Eng Perform 2014;23:1917–28. https://doi.org/10.1007/s11665-014-0958-z.
[7] Kok Y, Tan XP, Wang P, Nai MLS, Loh NH, Liu E, et al. Mater Des 2018;139:565–86. https://doi.org/10.1016/j.matdes.2017.11.021.
[8] Chen S, Gao H, Zhang Y, Wu Q, Gao Z, Zhou X. J Mater Res Technol 2022;17:2950–74. https://doi.org/10.1016/j.jmrt.2022.02.054.
[9] Sanaei N, Fatemi A. Prog Mater Sci 2021;117:100724. https://doi.org/10.1016/j.pmatsci.2020.100724.
[10] Persenot T, Burr A, Martin G, Buffiere J, Dendievel R, Maire E. Int J Fatigue 2019;118:65–76. https://doi.org/10.1016/j.ijfatigue.2018.08.006.
[11] Sanaei N, Fatemi A. Theor Appl Fract Mech 2020;108:102638. https://doi.org/10.1016/j.matdes.2019.108091.
[12] Sanaei N, Fatemi A. Mater Sci Eng A 2020;785:139385. https://doi.org/10.1016/j.msea.2020.139385.
[13] Gong H, Rafi K, Gu H, Janaki Ram GD, Starr T, Stucker B. Mater Des 2015;86:545–54. https://doi.org/10.1016/j.matdes.2015.07.147.
[14] Greitemeier D, Dalle Donne C, Syassen F, Eufinger J, Melz T. Mater Sci Technol 2016;32:629–34. https://doi.org/10.1179/1743284715Y.0000000053.
[15] Yadollahi A, Mahtabi MJ, Khalili A, Doude Jr HR, Newman JC. Fatigue Fract Eng Mater Struct 2018;41:1602–14. https://doi.org/10.1111/ffe.12799.
[16] Gockel J, Sheridan L, Koerper B, Whip B. Int J Fatigue 2019;124:380–8. https://doi.org/10.1016/j.ijfatigue.2019.03.025.
[17] Schneller W, Leitner M, Leuders S, Sprauel JM, Grün F, Pfeifer T, et al. Addit Manuf 2021;39:101688. https://doi.org/10.1016/j.addma.2020.101688.
[18] Wang J, Zhang M, Wang B, Tan X, Wu WJ, Liu Y, et al. Int J Fatigue 142 2021:105894. https://doi.org/10.1016/j.ijfatigue.2020.105894.
[19] Romano S, Brückner-Foit A, Brandao A, Gumpinger J, Ghidini T, Beretta S. Eng Fract Mech 2018. https://doi.org/10.1016/j.engfracmech.2017.11.002.
[20] Siddique S, Imran M, Walther F. Int J Fatigue 2017;94:246–54. https://doi.org/10.1016/j.ijfatigue.2016.06.003.
[21] Plessis AD, le Roux SG. Addit Manuf 2018;24:125–36. https://doi.org/10.1016/j.addma.2018.09.014.
[22] Sanaei N, Fatemi A, Phan N. Mater Des 2019;182:108091. https://doi.org/10.1016/j.matdes.2019.108091.
[23] Hamidi Nasab M, Romano S, Gastaldi D, Beretta S, Vedani M. Addit Manuf 2020;34:100918. https://doi.org/10.1016/j.addma.2019.100918.
[24] Lee S, Pegues JW, Shamsaei N. Int J Fatigue 2020;141:105856. https://doi.org/10.1016/j.ijfatigue.2020.105856.
[25] Karlsson J, Snis A, Engqvist H, Lausmaa J. J Mater Process Technol 2013;213(12):2109–18. https://doi.org/10.1016/j.jmatprotec.2013.06.010.
[26] Plessis AD, Yadroitsev I, Yadroitsava I, Roux SGL. 3D Print Addit Manuf 2018;5:227–47. https://doi.org/10.1089/3dp.2018.0060.
[27] Quan Z, Larimore Z, Qin X, Yu J, Mirotznik M, Byun JH, et al. Compos Sci Technol 2016;131:48–60. https://doi.org/10.1016/j.compscitech.2016.05.015.
[28] Nafar Dastgerdi J, Miettinen A, Parkkonen J, Remes H. Compos Struct 2018;194:292–301. https://doi.org/10.1016/j.compstruct.2018.04.022.
[29] Plessis AD, Yadroitsava I, Yadroitsev I. Mater Des 2020;187:108385. https://doi.org/10.1016/j.matdes.2019.108385.
[30] Choo H, Koehler MR, White LP, Ren Y, Morin D, Garlea E. Mater Sci Eng A 2020;791:139637. https://doi.org/10.1016/j.msea.2020.139637.
[31] Ghods S, Schur R, Schultz E, Pahuja R, Montelione A, Wisdom C, et al. Materialia 2021;15:100992. https://doi.org/10.1016/j.mtla.2020.100992.
[32] Kim FH, Moylan SP, Garboczi EJ, Slotwinski JA. Addit Manuf 2017;17:23–38. https://doi.org/10.1016/j.addma.2017.06.011.
[33] Heim K, Bernier F, Pelletier R, Lefebvre L-P. Case Stud Nondestruct Test Eval 2016;6:45–52. https://doi.org/10.1016/j.csndt.2016.09.002.
[34] Romano S, Brandão A, Gumpinger J, Gschweitl M, Beretta S. Mater Des 2017;131:32–48. https://doi.org/10.1016/j.matdes.2017.05.091.
[35] Tammas-Williams S, Withers PJ, Todd I, Prangnell PB. Sci Rep 2017;7:7308. https://doi.org/10.1038/s41598-017-06504-5.
[36] Romano S, Nezhadfar PD, Shamsaei N, Sei M, Beretta S. Theor Appl Fract Mech 2020;106:102477. https://doi.org/10.1016/j.tafmec.2020.102477.
[37] Nasab MH, Gastaldi D, Lecis NF, Vedani M. Addit Manuf 2018;24:373–7. https://doi.org/10.1016/j.addma.2018.10.011.
[38] Hu YN, Wu SC, Withers PJ, Zhang J, Bao HYX, Fu YN, et al. Mater Des 2020;192:108708. https://doi.org/10.1016/j.matdes.2020.108708.
[39] Wan HY, Luo YW, Zhang B, Song ZM, Wang LY, Zhou ZJ, et al. Int J Fatigue 2020;137:105654. https://doi.org/10.1016/j.ijfatigue.2020.105654.
[40] Barricelli L, Beretta S. Eng Fract Mech 2021;256:107983. https://doi.org/10.1016/j.engfracmech.2021.107983.
[41] Persenot T, Burr A, Dendievel R, Buffiere J, Maire E, Lachambre J, et al. Materialia 2020;9:100589. https://doi.org/10.1016/j.mtla.2020.100589.
[42] Plessis AD, Beretta S. Addit Manuf 2020;35:101424. https://doi.org/10.1016/j.addma.2020.101424.
[43] Natali S, Brotzu A, Pilone D. Materials 2019;12:3867. https://doi.org/10.3390/ma12233867.
[44] Strano G, Hao L, Everson RM, Evans KE. J Mater Process Technol 2013;213:589–97. https://doi.org/10.1016/j.jmatprotec.2012.11.011.
[45] Kasperovich G, Haubrich J, Gussone J, Requena G. Mater Des 2016;105:160–70. https://doi.org/10.1016/j.matdes.2016.05.070.
[46] Romano S, Brückner-Foit A, Brandao A, Gumpinger J, Ghidini T, Beretta S. Eng Fract Mech 2018;187:165–89. https://doi.org/10.1016/j.engfracmech.2017.11.002.
[47] Masuo H, Tanaka Y, Morokoshi S, Yagura H, Uchida T, Yamamoto Y, et al. Int J Fatigue 2018;117:163–79. https://doi.org/10.1016/j.ijfatigue.2018.07.020.
[48] Pessard E, Lavialle M, Laheurte P, Didier P, Brochu M. Int J Fatigue 2021;149:106206. https://doi.org/10.1016/j.ijfatigue.2021.106206.
[49] Murakami Y, Takahashi K, Yamashita T. Jpn Soc Mech Eng, Part A 1997;63:1612–9. https://doi.org/10.1299/kikaia.63.1612.
[50] Sanaei N, Fatemi A. Eng Fract Mech 2021;244. https://doi.org/10.1016/j.engfracmech.2021.107541.Townsend A, Senin N, Blunt L, Leach R, Taylor J. Precis Eng 2016;46:34–47. https://doi.org/10.1016/j.precisioneng.2016.06.001.
[51] Schneller W, Leitner M, Pomberger S, Grün F, Leuders S, Pfeifer T, et al. Addit Manuf 2021;40:101930. https://doi.org/10.1016/j.addma.2021.101930.
[52] Murakami Y, Endo M. Int J Fatigue 1993;16:163–82. https://doi.org/10.1016/0142-1123(94)90001-9.
[53] Rao JH, Zhang Y, Zhang K, Wu X, Huang A. Mater Des 2019;182:108005. https://doi.org/10.1016/j.matdes.2019.108005.
[54] Murakami Y. Metal Fatigue: Effects of small defects and nonmetallic inclusions. Elsevier; 2002.
[55] Kuo CN, Chua CK, Peng PC, Chen YW, Sing SL, Huang S, et al. Virtual Phys Prototyp 2019;15:120–9. https://doi.org/10.1080/17452759.2019.1698967.
[56] Everitt BS, Skrondal A. The Cambridge Dictionary of Statistics. Cambridge University Press; 2010.
[57] Biswal R, Syed AK, Zhang X. Addit Manuf 2018;23:433–42. https://doi.org/10.1016/j.addma.2018.08.024.
[58] Suard M, Martin G, Lhuissier P, Dendievel R, Vignat F, Blandin JJ, et al. Addit Manuf 2015;8:124–31. https://doi.org/10.1016/j.addma.2015.10.002.
[59] Hooreweder BV, Apers Y, Lietaert K, Kruth JP. Acta Biomater 2017;47:193–202. https://doi.org/10.1016/j.actbio.2016.10.005.

[60] Kruth JP, Levy G, Klocke F, Childs THC. Cirp Ann Manuf Technol 2007;56(2): 730–59. https://doi.org/10.1016/j.cirp.2007.10.004.
[61] Tian Y, Tomus D, Rometsch P, Wu X. Addit Manuf 2017;13:103–12. https://doi.org/10.1016/j.addma.2016.10.010.
[62] Wu ZK, Wu SC, Bao JG, Qian WJ, Karabal S, Sun W, et al. The effect of defect population on the anisotropic fatigue resistance of AlSi10Mg alloy fabricated by laser powder bed fusion. Int J Fatigue 2021;151:106317.
[63] Nezhadfar PD, Thompson S, Saharan A, Phan N, Shamsaei N. Structural integrity of additively manufactured aluminum alloys: Effects of build orientation on microstructure, porosity, and fatigue behavior. Addit Manuf 2021;47:102292.6.
[64] Chen B, Wu Z, Yan T, He Z, Sun B, Guo G, et al. Experimental study on mechanical properties of laser powder bed fused Ti-6Al-4V alloy under post-heat treatment. Eng Fract Mech 2022;261:108264. https://doi.org/10.1016/j.engfracmech.2022.108264.
[65] Åman M, Wada K, Matsunaga H, Remes H, Marquis G. Int J Fatigue 2020;135: 105560. https://doi.org/10.1016/j.ijfatigue.2020.105560.
[66] Chapetti MD, Tagawa T, Miyata T. Mater Sci Eng A 2003;356(1–2):236–44. https://doi.org/10.1016/S0921-5093(03)00136-9.
[67] Riemer A, Leuders S, Thöne M, Richard HA, Tröster T, Niendorf T. Eng Fract Mech 2014;120:15–25. https://doi.org/10.1016/j.engfracmech.2014.03.008.